AIAA 2014-0718
AIAA SciTech
13-17 January 2014, National Harbor, Maryland
52nd Aerospace Sciences Meeting

Experimental Simulation of Ducted Fan Acoustics at Very Small Scale

Alexander Truong[1] and Dimitri Papamoschou[2]
University of California, Irvine, Irvine, CA 92697

This study evaluated the feasibility of simulating the aerodynamics and acoustics of ducted fans using small-scale components (approximately 1/38th scale). Enabling technologies include high-definition stereolithography and high-performance, compact DC brushless motors used in model aircraft. The 70-mm ducted fan featured a 14-bladed rotor and 24 stators, and operated at fan pressure ratio of 1.15 and rotor tip Mach number of 0.61. Its operation was thus representative of turbofan engines with very large bypass ratio. The far-field acoustics were surveyed in the downward and sideline planes. The acoustic results of the isolated ducted fan compare favorably with past large-scale experiments. In addition, the project provided initial data on the shielding of ducted-fan noise using a surface that approximated the shape of the blended wing body airplane. The BWB-shaped shield featured removable inboard fins and a moveable elevon, and translated axially to enable various positions of the nacelle relative to the elevon trailing edge. The EPNL reduction on the downward plane ranged from 7.6 dB with the engine at its nominal location to 10.4 dB with the engine moved forward by one fan diameter. Sideline EPNL reduction was marginal with the fins off and reached about 3.0 dB with the fins installed. Upward deflection of the elevon improved moderately the shielding.

I. Introduction

The aviation community has set ambitious targets for the development of ultra-quiet commercial aircraft, encapsulated by NASA's N+2 and N+3 noise goals. Candidate propulsion schemes revolve around the high-bypass turbofan and the open rotor. Attainment of the noise goals requires not only improvements at the component level but also a systems integration approach for the design of the propulsion and the airframe. The shielding of engine noise by the airframe has been of particular interest, with recent efforts addressing fan inlet[1], jet[2,3], and open-rotor[4,5] noise. The blended wing body (BWB) airplane concept has been central to these efforts because its layout is amenable to innovative integration concepts and its aerodynamic efficiency is superior to that of conventional airplane designs[6]. The present work is an initial investigation of the scattering of fan noise from the BWB airframe, with emphasis on aft-emitted noise from a ducted fan at conditions similar to those of the geared turbofan (GTF).

Effective shielding of the GTF noise requires knowledge of the source characteristics. This impacts the entire aircraft design because decisions such as the placement of the engines, geometry of the elevon, and placement of the vertical fins are driven not only by aerodynamics but also acoustic considerations. Given that jet noise is significantly reduced in these high-bypass engines, prediction of the fan noise sources becomes critical. Fan noise, of course, has been the topic of numerous experimental, theoretical and computational investigations, some cited in this paper[7-14]. In particular, a series of studies conducted under the fan source diagnostic test (SDT) program resulted in extensive acoustic and flow field data[8,9] and proposed methods to reduce rotor-stator interaction noise[12-14]. Many of these tests were conducted in NASA state-of-the-art subscale (typically 22-in. diameter) rigs featuring pneumatic motors for powering the rotors and acoustic instrumentation that permits noise surveys as well as noise source location. These experiments are obviously very expensive. Due to the complexity and cost of the rotor hardware, only a small number of parameters can be varied within a reasonable budget. This limits the parameter space and the number of innovative ideas that can be explored.

Despite the extensive knowledge base on fan noise, there are scarce data on the fan noise characteristics of GTF-type engines which have lower fan pressure ratio and lower rotor tip Mach number than those emphasized in past studies. Experimental approaches to simulate fan noise have included the ultrasonic configurable fan artificial noise

[1] Junior Specialist, Department of Mechanical and Aerospace Engineering, adtruong@uci.edu, Member AIAA.
[2] Professor, Department of Mechanical and Aerospace Engineering, dpapamos@uci.edu, Fellow AIAA.

source (UCFANS) which uses electrostatic actuators in a no-flow-through nacelle[15]. This intricate simulator features monopole and dipole actuator configurations that reproduce the frequency and modal content of blade passing frequency tones. However, it is not clear that the UCFANS noise source can reproduce accurately the directivity of the fan tones and broadband noise. Knowledge of this directivity is essential for designing and optimizing the shielding configuration. Recognizing this need, the present exploratory investigation was initiated with the support of the Boeing Flight Sciences Technology organization.

The advent of stereolithographic fabrication methods enables the three-dimensional "printing" of complex, small-scale objects with high resolution. For an intricate design like a propeller, the manufacturing costs are orders of magnitude lower than fabricating the same article using conventional machining. This would permit the investigation of a large number of concepts at small cost, identifying promising configurations that may merit testing at larger scale and filtering out ideas that do not show promise. The rapid-prototyping approach has been used successfully with jet noise testing of realistic nozzle configurations[2]. More recently, initial open-rotor experiments were conducted in our facilities using rapid-prototyped propellers powered by high-performance DC motors[5]. These very small scale experiments required the rotor to spin at full-scale tip speeds to obtain a realistic acoustic assessment, and demonstrated the potential for studying the acoustics of the rotor in isolation and in the presence of a surface simulating the airframe.

The goal of this study is to improve the BWB noise shielding predictions for aft-emitted fan noise, by using a source that captures the physics of fan noise generation and simulates with good fidelity the fan exhaust noise signature (tonal content, modal content, broadband noise, directivity) of a modern high-bypass turbofan engine. The proposed low-cost, subscale approach enables coverage of a large parameter space in terms of fan properties (e.g., rotor/stator count), shield geometry, and engine placement. The results can thus guide large-scale tests and provide inputs to predictive modeling. The approach could complement the aforementioned method of UCFANS. The paper describes the acoustic characteristics of ducted fans at very small scale, fabricated using advanced stereolithography and driven by powerful DC motors to attain realistic operating conditions. Initial results on noise shielding using a BWB-shaped shield are also reported.

II. Experimental Apparatus

A. Ducted Fan Design

The specifications of the ducted fan are summarized in Table 1, and several views of the design are shown in Figs. 1-3. Various design elements of the rotor and stators were extracted from published reports, particularly Refs. 8, 10, and 11. The design was then modified to adapt to the low fan pressure ratio operation of a geared turbofan (GTF) simulation and to accommodate the small scale of the experiment. Ducted fan momentum theory was used to set the rotor diameter and optimize the nacelle design for the available power of high-performance DC motors. Accordingly, a nacelle with an inlet diameter of 70 mm and exit-to-inlet area ratio of 0.56 was selected. A bell-mouth entry for the nacelle was chosen to prevent flow separation in the static test environment.

The rotor and stator counts were 14 and 24, respectively, giving a rotor-stator ratio of 0.58. The relatively low counts were selected for manufacturing considerations; however, having gained experience with the manufacturing process, higher counts will be possible in the future. Experimentation with the rotor pitch angle and solidity was necessary to arrive at a satisfactory aerodynamic performance, as measured by pressure sensors. Blade element analysis, in conjunction with momentum theory, assisted this effort.

The nacelle (including the stators) and rotor were manufactured by Fineline Corporation using 3D Systems' Viper High Resolution SLA machine. The material was Accura 60 resin by 3D Systems with tensile strength of ~60 MPa. The nacelle features pressure ports for measuring the inlet static pressure and the outlet total pressure. The aerodynamic performance was assessed by these pressure measurements.

Table 1 Ducted Fan Specifications

	Parameter	Specifications
Nacelle	Fan inlet diameter	70.0 mm
	Fan exit diameter	71.0 mm
	Nacelle exit to inlet area ratio	0.56
	Design fan pressure ratio	1.15
	Input power	5.0 kW (6.7 hp)
Rotor	Overall design	Based on GE R4 fan
	Count	14
	Diameter	69.2 mm (0.4 mm tip clearance)
	Design RPM	57000
	Design Tip Mach	0.61
	Hub-to-Tip Ratio	0.42
	Solidity	1.34 at pitch line
	Blade Airfoil	NACA 65-Series
	Blade Camber	56.6^o (hub) to 6.2^o (tip)
	Blade Pitch Angle	51.6^o (hub) to 28.3^o (tip)
	Blade Thickness/Chord Ratio	0.081 (hub) to 0.028 (tip)
Stator	Overall design	Radial vane, based on low-count SDT configuration
	Count	24
	Solidity	2.21 (hub) to 1.04 (tip)
	Blade Airfoil	NACA 65-Series
	Blade Camber	42.2^o (hub) to 40.6^o (tip)
	Blade Thickness/Chord Ratio	0.0707 (hub) to 0.0698 (tip)

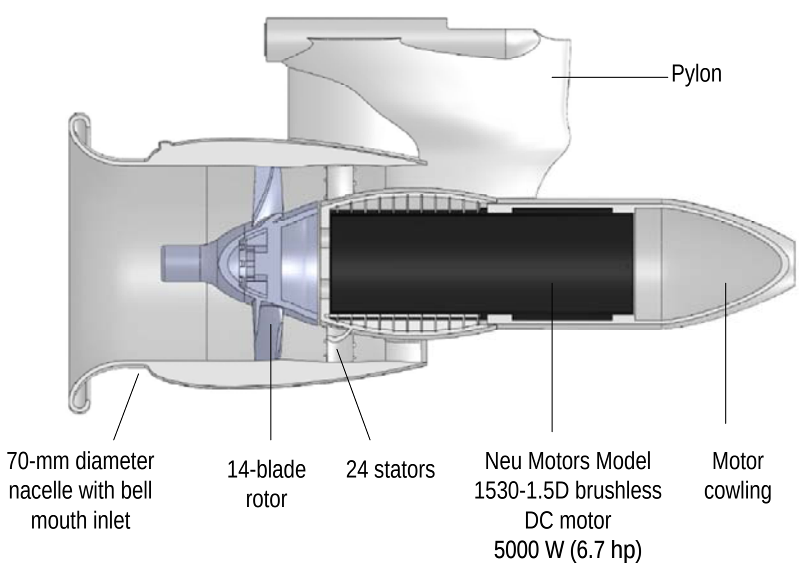

Fig. 1 Overview of ducted fan design.

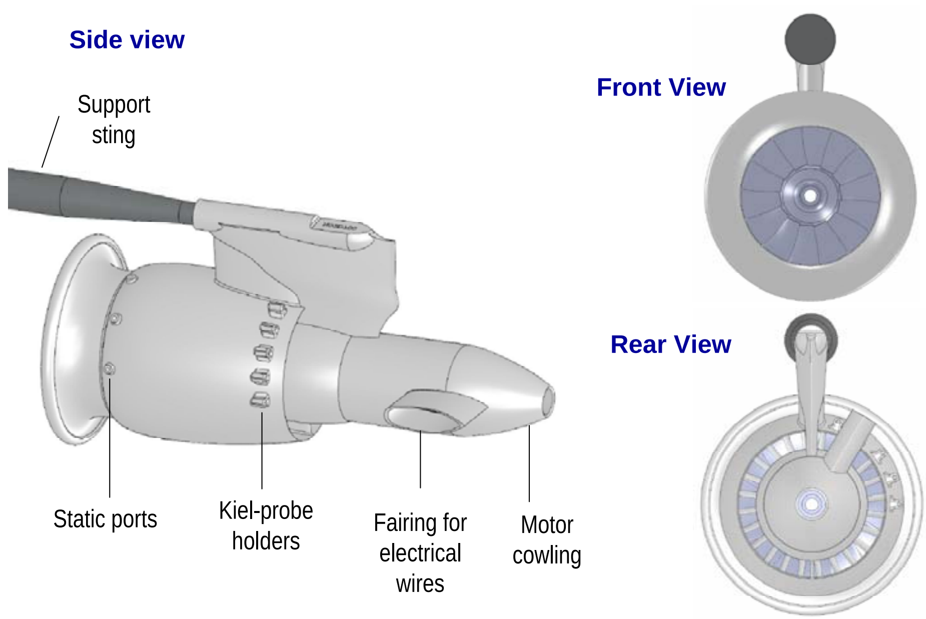

Fig. 2 Various views of ducted fan.

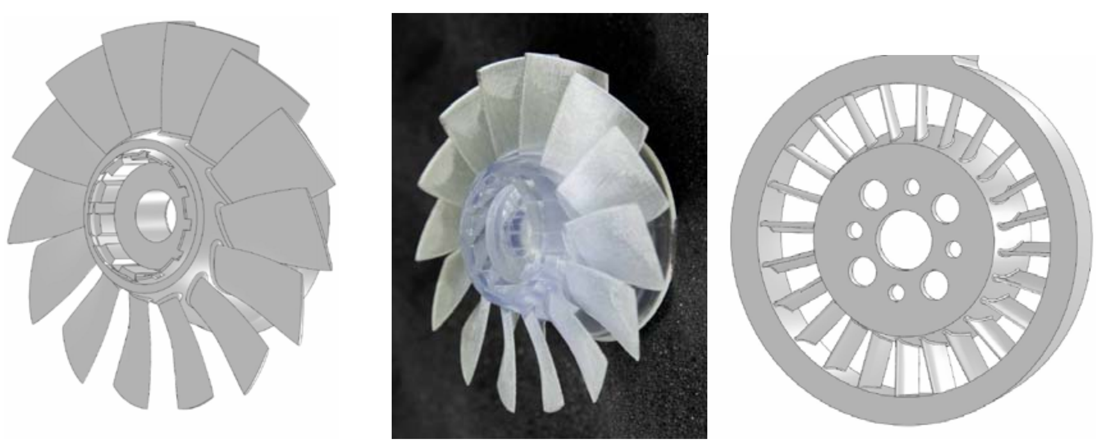

Fig. 3 a) CAD drawing or rotor; b) manufactured rotor; c) CAD drawing of stator assembly. Central disk contains holes for motor mounting.

B. Shield

The flat-plate shield approximated the planform of Boeing's BWB 2025-0009A design[16]. Figure 4 shows the approximation and scaling down, and Fig. 5 shows the actual UCI design. The shield was fabricated from 1/8-in. aluminum plate. The chord and span were truncated relative to the BWB 2025-0009A design. The UCI design featured removable inboard fins, placed at 39.6^o dihedral, and movable elevon. The shield could translate axially on rails to adjust the axial position of the ducted fan relative to the shield trailing edge. The design also featured tip extensions to achieve the full (scaled down) span; however, because of resource limitations the extensions were not included in the test matrix.

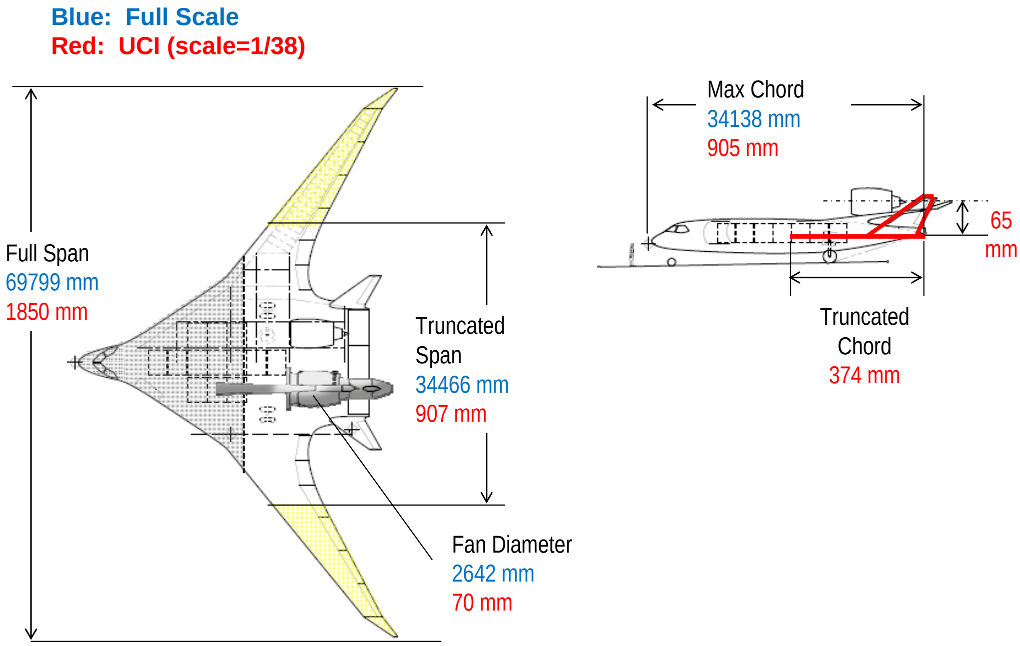

Fig. 4 Full-scale and UCI shield dimensions based on Boeing's BWB 2025-0009A planform [16]. Scale factor=38.

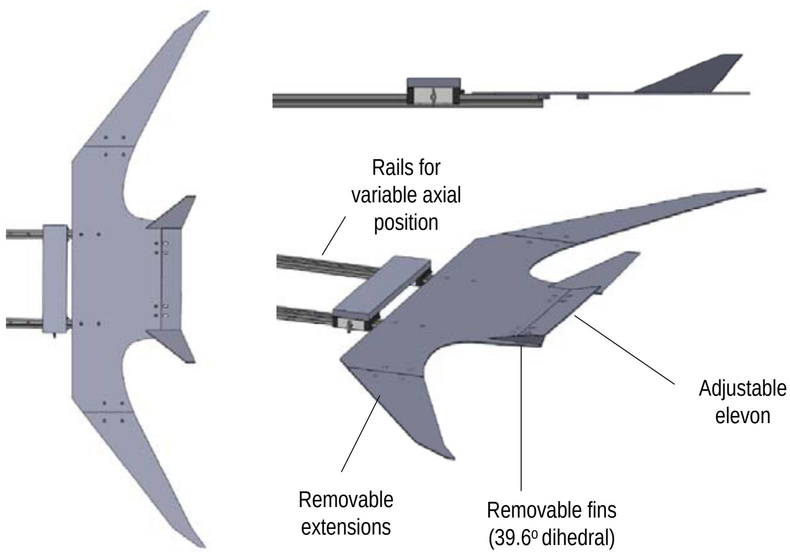

Fig. 5 Flat-plate design of shield based on BWB 2025-0009A planform.

C. Power Components

The rotor was powered by a high-performance brushless DC motor (Neu Motors, Model 1530-1.5D) which can attain surge power of 5.0 kW. The motor has an RPM/Volt (Kv) rating of 1350, meaning that it can spin at an RPM of ~60,000 at the maximum rated voltage of 44V. The motor was controlled using Castle Creations Phoenix 160-Amp electronic speed controller (ESC). Power to the speed controller was supplied by two 6S (22.2-Volt) lithium-ion polymer (Lipo) battery connected in series with a discharge rate of 30c and a capacity of 8300 mAh. The speed controller was controlled by a Spektrum AR6200 DSM2 six-channel receiver connected wirelessly to a Spektrum DX7 2.4 GHz seven-channel radio. The receiver was powered by a Castle Creations battery eliminator circuit (BEC PRO). The power components and their installation are depicted in Fig. 6.

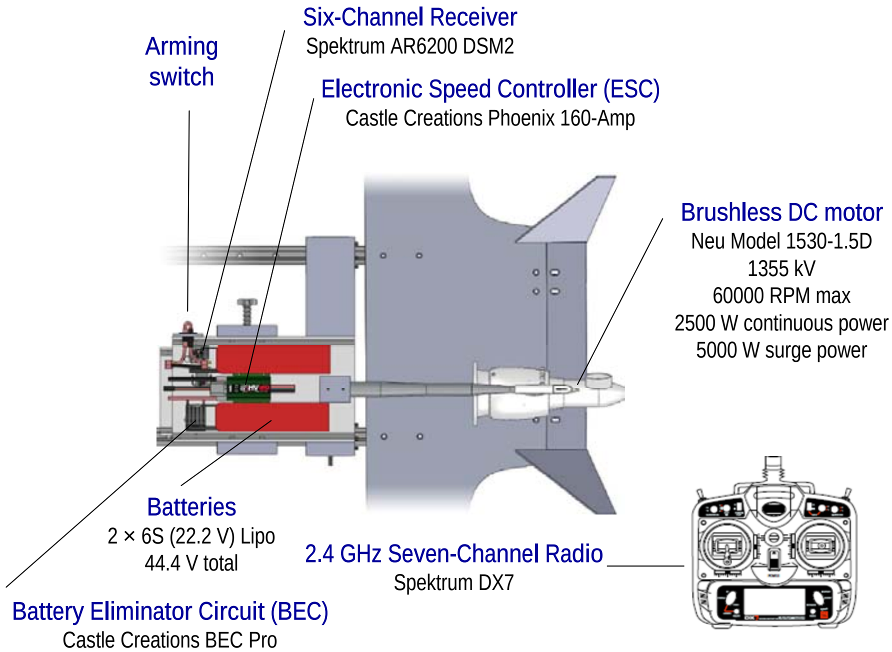

Fig. 6   Principal power components and their installation.

D. Complete Assembly

A picture of the completed assembly is shown in Fig. 7.   The power cables connecting to motor to the battery (carrying ~150 Amps and 44 Volts) were short, placing the nacelle relatively close to the power components and support structure.   While this was not ideal aerodynamically, the primary consideration here was safety given the very high currents involved.   Future designs may relax this constraint and place the nacelle in an aerodynamically cleaner environment.   Inlet pressure measurements indicated very slight non-uniformity of the flow entering the nacelle.

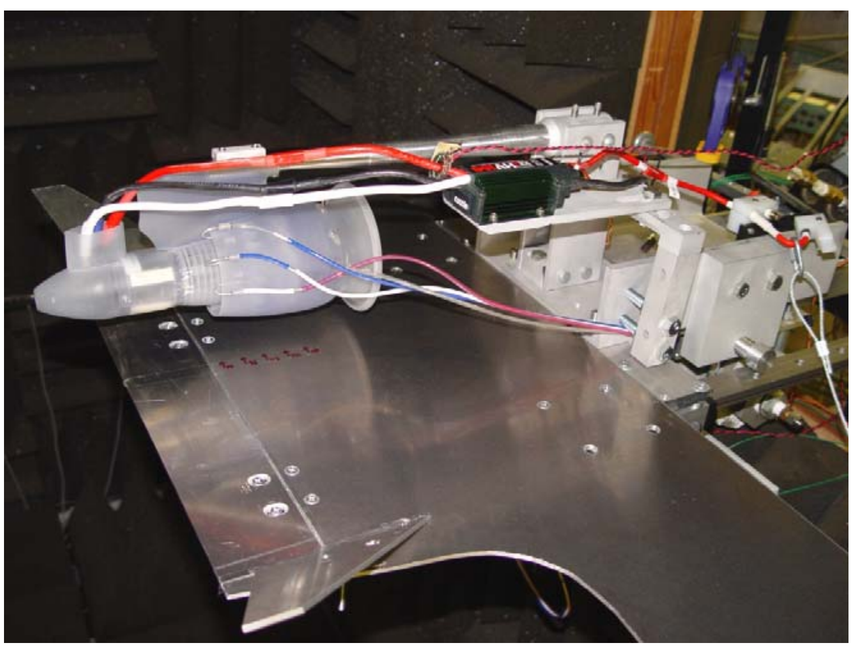

Fig. 7 Picture of complete assembly.

III. Diagnostics

A. Pressure Instrumentation

The total pressure near the fan exit plane was measured using three Kiel probes arranged at different azimuthal locations, as shown in Fig. 8. The Kiel (total-pressure) probes were individually connected to pressure transducers (Setra Model 209, 0-5 psig). Multiple probes were used to mitigate the effects of stator wakes on the total pressure measurement. The maximum of the three readings was used to determine the fan pressure ratio (FPR). The aerodynamic performance of the ducted fan was assessed based on this measurement of FPR.

In addition to the Kiel probes, static pressure ports were available at various azimuthal locations for measuring the inlet static pressure (see also Fig.8). One transducer was available for the static pressure measurements (Setra Model 2671, 0-25 in. WC). There was no significant variability of the inlet pressure with azimuthal location (indicating uniformity of the entry flow) and the value of the inlet pressure was consistent with the total pressure measurement.

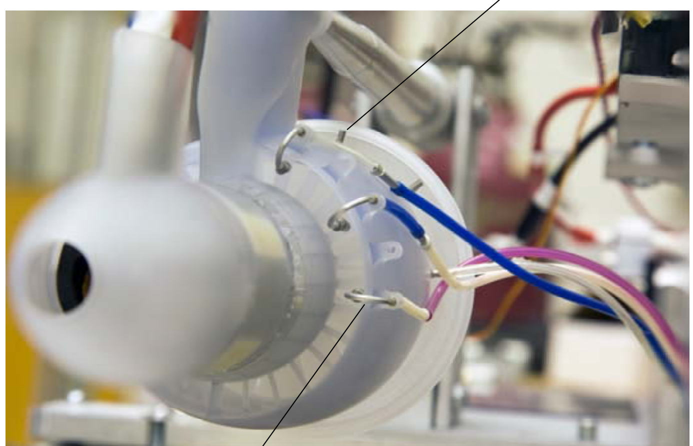

Fig. 8 Pressure diagnostics.

B. RPM Measurement

Rotor speed was determined by detection of the pulsation of the electrical load from the electronic speed controller (ESC) to the motor, using a ferrite toroid Hall effect sensor as shown in Fig. 9. The ESC sends a pulse-width modulated (PWM) waveform to the motor. The pulses are emitted at the commutation frequency, f_c , which is the frequency of the switching of the polarity of the magnets to keep the motor turning. The pulse width controls the power to the motor. The raw signal voltage from the Hall effect sensor is reduced to levels tolerated by the data acquisition system using a voltage divider circuit, and is then fed to a low-pass filter through a buffer. The low-pass filter attenuates the fast switching PWM component of the signal, while the buffer prevents unacceptable loading of the voltage divider circuit by the low-pass filter circuit. The spectrum of the signal is then computed using a Fast Fourier Transform. The highest peak of the spectrum is at the commutation frequency. Conversion from the commutation frequency f_c (Hz) to RPM is given by the formula RPM=$f_c \cdot 60 \cdot 2/N_p$, where N_p is the number of magnetic poles in the motor. The Neu 1530 motor has four poles, for which RPM=$30 f_c$. This method enabled real-time measurement of the RPM for each acoustic test run (the RPM signal was collected simultaneously with the microphone signals). The RPM measurement was in perfect agreement with data downloaded from the ESC once an experimental sequence was complete.

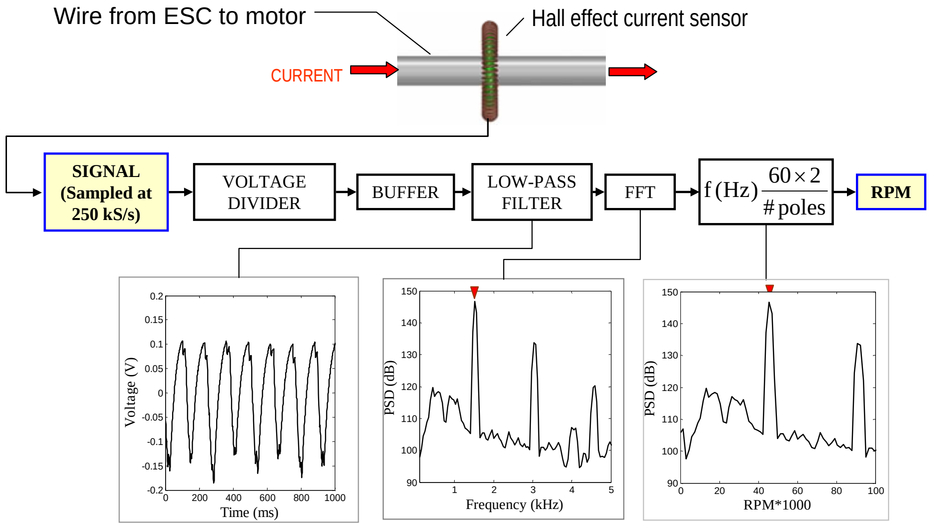

Fig. 9 RPM measurement.

C. Acoustic Measurement and Processing

Acoustic measurements were conducted inside an anechoic chamber at the UC Irvine's Aeroacoustics Facility, depicted in Figs. 10 and 11. Twenty-three 3.2-mm condenser microphones (Bruel & Kjaer, Model 4138) with a frequency response of 140 kHz were used to survey the far-field acoustics. The microphones were arranged twelve on a downward arm (azimuth angle $\phi=0^{o}$) and eleven on a sideline arm (azimuth angle $\phi=60^{o}$). The polar angle θ is defined from the center of the fan exit plane relative to the downstream rotor axis, as shown in Fig. 10. Its approximate range was 15^{o} to 110^{o} for the downward arm, and 15^{o} to 100^{o} for the sideline arm. The minimum microphone-to-nacelle distance was 0.8 m, or 11.4 fan diameters. This places the microphones in the acoustic far field for the frequency range relevant to aircraft noise (i.e., higher than 50 Hz full scale). With the shield installed, the sideline measurements were conducted on the side of the fin proximal to the nacelle (Fig. 10).

The microphones were connected, in groups of four, to six conditioning amplifiers (Bruel & Kjaer, Model 2690-A-0S4). The 23 outputs of the amplifiers were sampled simultaneously, at 250 kHz per channel, by three eight-channel multi-function data acquisition boards (National Instruments PCI-6143). A 24^{th} output channel was assigned to the RPM sensor. National Instruments LabView software was used to acquire the signals. The temperature and humidity inside the anechoic chamber were recorded to enable computation of the atmospheric absorption.

The sampling rate for each microphone was 250000 samples/second, and the number of samples for each test run was 262144 per microphone. The narrowband sound pressure level spectra were computed with a Fast Fourier Transform with size of 8192, giving a frequency resolution of 30.5 Hz. The SPL narrowband spectra were corrected for actuator response, free-field correction, and atmospheric absorption, resulting into lossless spectra. The overall sound pressure level (OASPL) was calculated through integration of the lossless SPL spectrum. In addition, the full-scale, 1/3-octave spectrum was calculated from the lossless narrowband spectrum after dividing the frequency vector by the scale factor of 38. The lab-scale SPL narrowband spectrum, lab-scale OASPL, and full-scale 1/3-octave spectrum, are referenced to a distance of 305 mm (12 in.) from the exit of the ducted fan.

The flyover perceived noise level (PNL) and effective perceived noise level (EPNL) calculations were based on the narrowband lossless SPL spectra. Takeoff flight profiles were defined with representative values of altitude, climb angle, engine angle of attack, and flight Mach number for the BWB. Referring to Fig.12, the flight path horizontal (x') and vertical (y') coordinates were defined as functions of observer time t in 0.5-second intervals. Having defined a flight path ($x'(t)$, $y'(t)$) and an observer position, the calculation of PNL(t) and EPNL for a given run comprises the following steps.

- Scaling up of the SPL spectra (division of frequency vector by the scale factor) and extrapolation to unresolved frequencies using a decay of 12 dB per decade (a drop that reflects the roll-out of the broadband part of the ducted fan spectrum).
- Calculation of the retarded flight path ($x(t)$, $y(t)$) and associated observer polar angle $\theta(t)$ with respect to the downstream engine axis.

- For each observer time t, selection of the full-scale spectrum SPL(f, $\theta(t)$). This step involves interpolation between measured polar angles and moderate extrapolation outside the range of measured polar angles θ.
- Geometric scaling of the SPL(f, $\theta(t)$) to the source-observer distance.
- Atmospheric attenuation for the source-observer distance, using the relations of Bass *et al.* [17]
- Doppler shift of the spectra, using the approach of McGowan and Larson[18].
- Computation of the 1/3-octave spectrum versus flyover time.
- Noy weighting and calculation of PNL(t) according to FAR36 [19], including tone correction.
- Determination of maximum PNL (PNLM), duration correction (D), and EPNL=PNLM+D according to FAR36.

The takeoff flight parameters used for the evaluation of PNL(t) and EPNL are shown in Fig. 12.

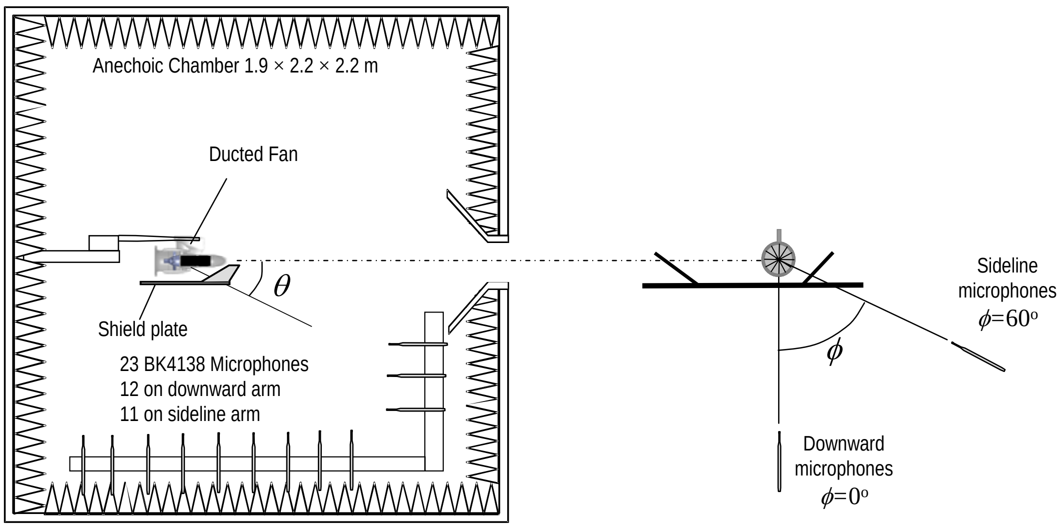

Fig. 10 Aeroacoustic test setup.

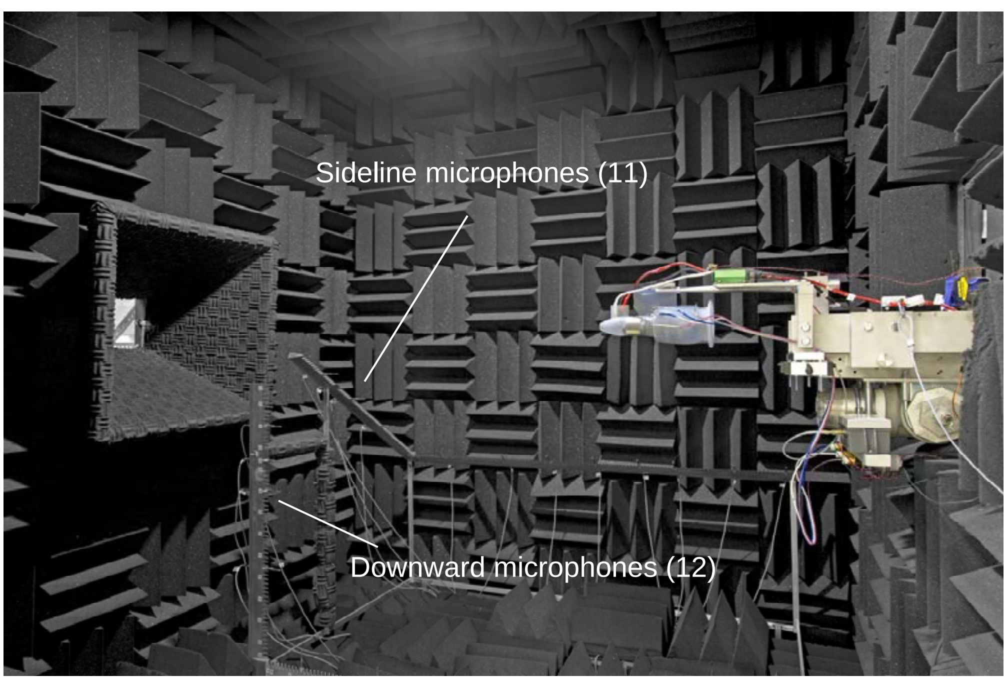

Fig. 11 Picture of isolated ducted fan tested inside anechoic chamber.

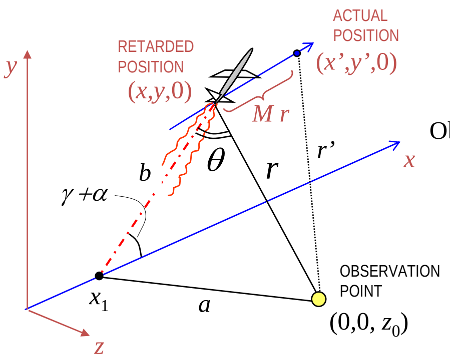

Aircraft flying with Mach number M, angle of attack α, and climb angle γ

Observation distance and polar emission angle

$$r' = \sqrt{x'^2 + y'^2 + z_0^2}$$

$$\boxed{\begin{aligned} r &= \sqrt{x^2 + y^2 + z_0^2} \\ \tan(\theta/2) &= \sqrt{\frac{(p-b)(p-r)}{p(p-a)}} \end{aligned}}$$

where

$$x_1 = x - y/\tan(\gamma+\alpha)$$

$$a = \sqrt{x_1^2 + z_0^2}$$

$$b = y/\sin(\gamma+\alpha)$$

$$p = \frac{1}{2}(a+b+r)$$

CONDITIONS FOR EVALUATON OF PNL		
	SIDELINE	DOWNWARD
Lateral distance, z_o=	1476 ft	0 ft
Altitude at x=0	1000 ft	2104 ft
Angle of attack, a=	13.4 deg	13.9 deg
Climb angle, g=	9.5	2.3
Flight Mach, M=	0.217	0.220

Fig. 12 Geometric relations and takeoff profiles used in the calculation of PNL.

IV. Test Matrix

For all the conditions covered in this report, the RPM was 57200 ±1%. The rotor tip Mach number was 0.61 ± 1%. Maximum Kiel probe reading was 2.2 psig, which translates to FPR=1.15, rotor induced velocity of 87 m/s, fan exit velocity of 155 m/s, and power output of 4400 W (5.9 hp). The calculated power output is consistent with the motor input power of 5000 W and a conversion efficiency of 88%.

The test matrix comprised variations in the ducted fan axial position and in the shield elevon angle. In addition, tests were conducted with the fins installed and removed. Figure 13 illustrates the axial movement of the ducted fan in terms of the trailing edge distance, X_{te}, normalized by the exit fan diameter, $D_{fan,\ exit}$. The nominal location $X_{te}/D_{fan,\ exit}$=1.1 was inferred from the BWB 2025-0009A drawing. All nacelle positions are at or upstream of this nominal location.

The vertical and spanwise positions of the nacelle were fixed throughout the tests. They had the values Y=65 mm and Z=91 mm. Here Y is the distance between the nacelle axis and shield surface; and Z is the distance between the nacelle axis and vertical plane of symmetry of the shield. Normalized by fan exit diameter, these dimensions are $Y/D_{fan,\ exit}$=0.915 and $Z/D_{fan,\ exit}$=1.23

Table 2 lists the test points and includes estimates of EPNL to be reviewed in the following sections.

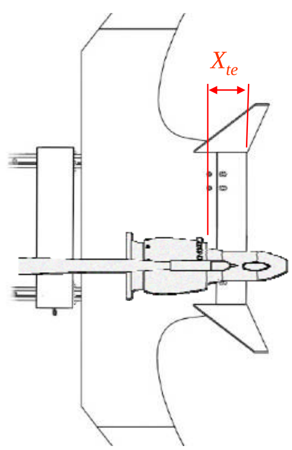

Nacelle Axial Position X_{te} = axial distance between fan exit plane and shield trailing edge		
X_{te} (mm)	$X_{te}/D_{fan\ exit}$	Notation
78	1.10	Nominal position*
96	1.35	0.26*D forward
114	1.60	0.50*D forward
149	2.10	1.00*D forward

* Based on BWB0009C drawing

Fig. 13 Axial movement of ducted fan.

Table 2 Test matrix including EPNL estimated values.

Experiment	$X_{te}/D_{fan,\ exit}$	Fins	Elevon angle (deg)	$EPNL_D$ (dB)	$EPNL_S$ (dB)	$\Delta EPNL_D$ (dB)	$\Delta EPNL_S$ (dB)
GTF0266	Isolated			79.02	80.63	0.00	0.00
GTF0273	0.00	OFF	0.0	71.52	79.33	-7.49	-1.30
GTF0283	0.26	OFF	0.0	70.10	79.27	-8.92	-1.36
GTF0293	0.50	OFF	0.0	69.35	78.85	-9.67	-1.77
GTF0303	1.00	OFF	0.0	69.11	78.61	-9.91	-2.01
GTF0318	0.00	ON	0.0	71.38	77.63	-7.64	-3.00
GTF0324	0.26	ON	0.0	70.33	77.94	-8.69	-2.69
GTF0334	0.50	ON	0.0	69.36	-	-9.66	-
GTF0344	1.00	ON	0.0	68.61	-	-10.41	-
GTF0359	0.00	ON	20.0	70.98	76.66	-8.04	-3.97
GTF0363	0.50	ON	20.0	70.52	-	-8.50	-
GTF0373	0.50	ON	-20.0	-	-	-	-

V. Acoustic Results

The acoustic results will be presented in multi-part figures, each figure showing comparisons that include the isolated ducted fan. The parts of each figure are as follows:

(a) Narrowband SPL spectra in laboratory scale, referenced to 12-in. arc, plotted for various polar angles and for the two azimuthal directions (downward and sideline).

(b) 1/3-octave spectra in full scale, referenced to 12-in. arc, plotted for various polar angles and for the two azimuthal directions (downward and sideline).

(c) Directivity of tones as detected from the narrowband spectra, referenced to 12-in. arc. Note that the tone amplitude depends on the spectral bandwidth (in this case 30.5 Hz), so these plots are meaningful for the directivity trends and for comparing difference cases.

(d) Directivity of selected 1/3-octave band levels (full-scale).

(e) "Integrated" noise metrics: directivity of OASPL (lab scale, referenced to 12-in arc); flyover PNL versus time; flyover PNL versus observer polar angle; and listing of the estimated EPNLs. In some instances the limited polar range of the microphones, combined with a complicated time history of PNL, did not allow resolution of the EPNL. In those cases, the EPNL value is displayed as zero.

A. Effects of Nacelle Axial Position and Fin Installation

The first set of comparisons involves the effect of engine axial location with fins on and off. Detailed acoustic results will be presented for only two engine positions. Summary results will include all positions. Figures 14 and present acoustic results for X_{te}=0 and 1.0D upstream of the nominal position, respectively. Each figure contains data with fins off and on.

Starting with Fig.14, part (a) shows the narrowband spectra for the isolated fan (red curves), installed fan at nominal location with fins off (blue curves), and installed fan at nominal location with fins on (green curves). The blade passing frequency (BPF) tones are evident in all of the figures; tones up to 7*BPF are discernible. The shield offers deep reductions in spectral levels in the downward direction and for polar angles greater than ~40^o. The downward spectra do not change significantly with the fins off or on. In the sideline direction, with the fins off, the shield does not produce significant reductions unless the polar angle is very large. With the fins on, the sideline reductions are notable for polar angles greater than ~60^o, but are not as deep as in the downward direction.

The corresponding 1/3-octave, full-scale spectra are shown in part (b) of Fig. 14. We note the same trends as for the narrowband spectra. Reductions become significant for full-scale frequency above ~200 Hz and become largely independent of frequency for full-scale frequency above ~1000 Hz. At angles near 90^o, the largest reductions are about 15 dB in the downward direction and 10 dB in the sideline direction (with fins on).

Part (c) of Fig. 16 plots the directivities of tones 1*BPF through 5*BPF. For the isolated fan, the 1*BPF tone peaks near the rotor plane, while the harmonics tend to peak in the aft (downstream) direction. In the downward direction, there is a consistently large suppression of the tones with installation of the shield. In the sideline direction, the reduction is moderate and the benefit of the fins is more pronounced for the 3*BPF and 5*BPF tones.

The directivities of 1/3-octave bands 10, 13, 14, 16, and 17 are presented in part (d) of Fig.14. The figure indicates the center frequencies and which tones fall within each octave band. Similar trends are observed as in part (c), with the sideline direction showing more consistent reductions with installation of the fins.

Part (e) of Fig. 14 includes the OASPL directivity, flyover PNL data, and EPNL estimates. In the downward direction, the OASPL is reduced by much as 12 dB with installation of the shield. Attachment of the fins raises moderately the downward OASPL levels; however, this is a low-frequency contribution that has minimal impact on the PNL. In the sideline direction, the beneficial effect of the fins on the OASPL is evident. The PNL(t) and PNL(θ) results in the downward direction show virtually identical results with fins on and off. In the sideline direction, the fins are shown to have a pronounced effect for observer polar angles greater than 50^o (corresponding to times prior to the occurrence of PNL_{max}). The estimated EPNL reductions are as follows. In the downward direction, the EPNL is reduced by 7.4 dB with the fins off and 7.6 dB with the fins on. In the sideline direction, the EPNL is reduced by 1.3 dB with the fins off and 3.0 dB with the fins on.

With the nacelle moving upstream one rotor diameter, Fig. 15, the aforementioned reductions are moderately accentuated but the overall trends remain similar. One important difference is the flyover PNL trends for the sideline direction with fins installed and for significant forward positions of the engine. See Figs. 15(e). As the engine moves upstream relative to the fin, the "shadow" zone created by the fin shifts to lower polar angles. As a result, the sideline flyover PNL(t) trend has an irregular shape with a dip surrounded by two peaks, reflecting the observer entering and exiting the shadow zone. Even though the peak PNL is suppressed substantially, the irregular shape of PNL(t) creates a significant duration penalty and in some cases prevented the calculation of EPNL (because the PNL_{max}-10 dB times could not be resolved for the measured range of polar angles). For the upstream-most engine location (1.0D forward of nominal), the reduction in downward EPNL is 10.4 dB (with fins on).

B. Effects of Elevon Angle

The next set of comparisons involves the effect of elevon angle on shielding, with the fins installed. Figure 16 compares the isolated fan (red lines), shielded fan with elevon at 0^o, and shielded fan with elevon at $+20^o$ (deflected up). The nacelle location is nominal. The effect of the upward elevon deflection is most clearly seen in the 1/3-octave band directivity, Fig. 16(d). Significant reductions (relative to the undeflected elevon) are noted for the lower octave bands and polar angles near 40^o. In terms of EPNL reduction (Fig. 16(e)), the +20 deg elevon deflection improves the downward reduction by 0.4 dB and the sideline reduction by 1.0 dB.

The effects of $\pm 20^o$ elevon deflections are compared in Fig. 17, for the nacelle at 0.5D upstream of nominal and fins installed. As expected, the negative deflection reduces shielding and the positive deflection improves shielding. Unfortunately, for this set of runs, the EPNL was not resolved so the EPNL benefit cannot be directly assessed.

C. EPNL Trends

To encapsulate the main EPNL trends, Figure 18 plots the resolved EPNL reductions versus nacelle axial position for the downward and sideline directions. The elevon angle is zero. For the downward direction, the reductions are very substantial, starting at ~7.5 dB with the nacelle at nominal position and reaching ~10 dB with the nacelle one diameter forward of nominal. A point of diminishing returns is reached at about 0.5D upstream of nominal. The fins have very small impacts on the downward EPNL reductions.

For the sideline direction, EPNLs with fins on were resolved only for the first two nacelle positions. With the fins off, the sideline EPNL reduction is 1.3 dB with the nacelle at nominal position and reaches 2.0 dB with the nacelle one diameter upstream of nominal. With the fins on, the sideline EPNL reduction becomes about 3.0 dB with the nacelle near the nominal location. In other words, the benefit of the fins on cumulative (takeoff+sideline) EPNL is estimated at about 1.5 dB. Although this number is small, it should be noted that the fin geometry was not optimized for noise reduction and subtle changes in the fin layout could result in significant improvements in sideline EPNL.

The resolved EPNL values are also listed in Table 2. The following convention is used: $EPNL_D$ = downward EPNL; $EPNL_S$=sideline EPNL.

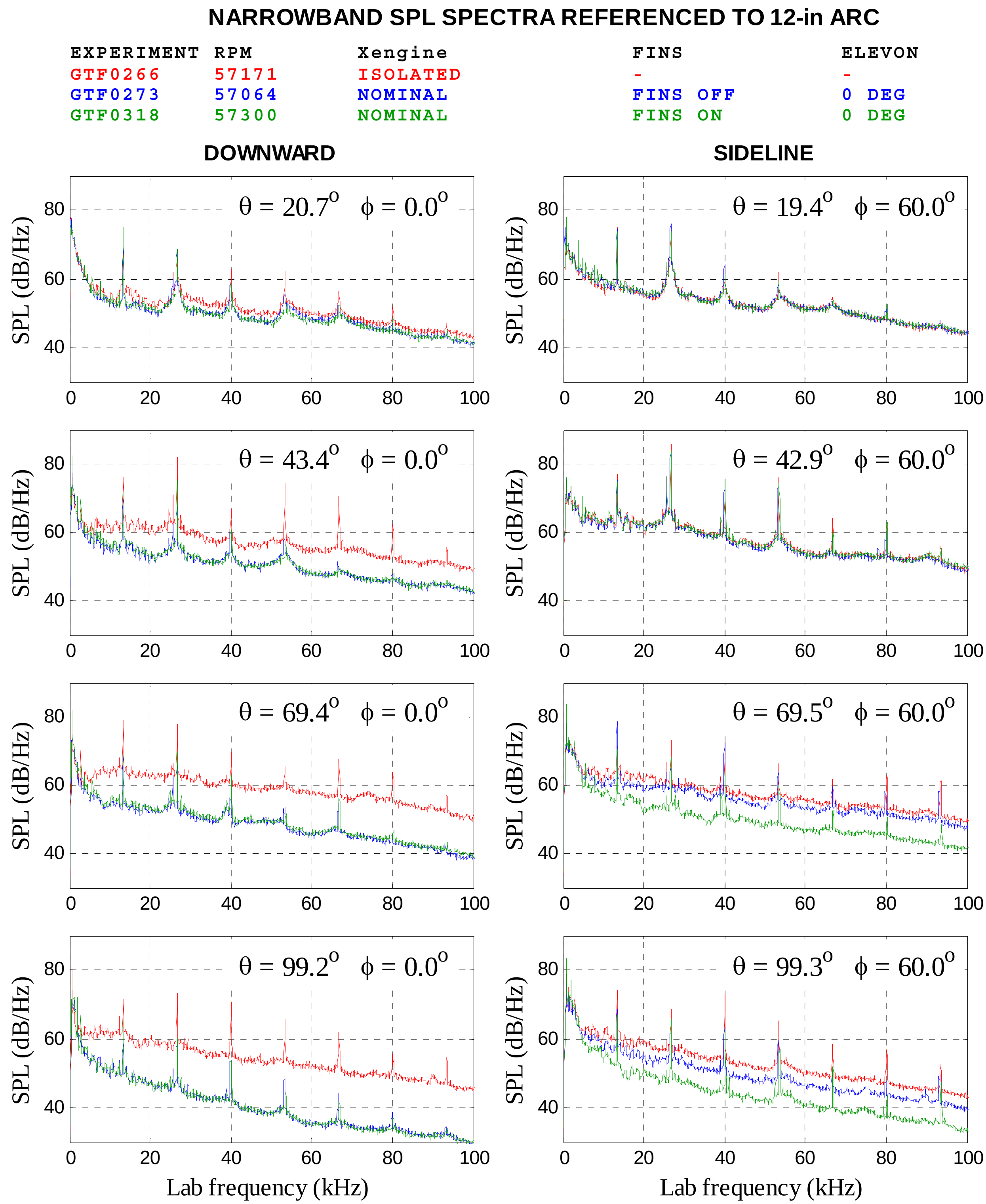

Fig. 14(a) **Narrowband SPL spectra for: isolated ducted fan (red); shielded ducted fan with fins removed (blue); shielded ducted fan with fins installed (green). Engine at nominal axial location. Elevon angle = 0°.**

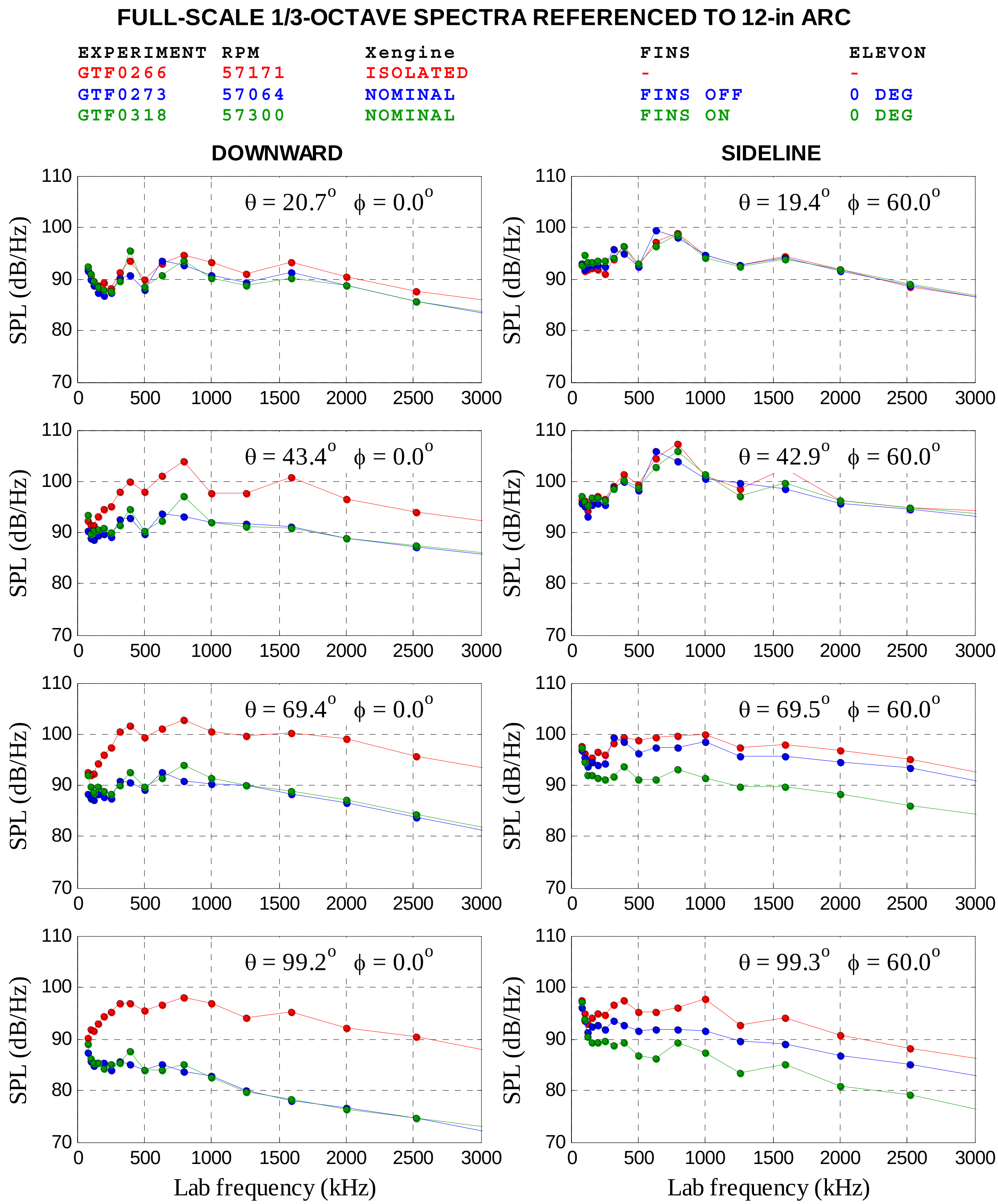

Fig. 14(b) **Full-scale 1/3-octave spectra for: isolated ducted fan (red); shielded ducted fan with fins removed (blue); shielded ducted fan with fins installed (green). Engine at nominal axial location. Elevon angle = 0°.**

EXPERIMENT	RPM	Xengine	FINS	ELEVON
GTF0266	57171	ISOLATED	-	-
GTF0273	57064	NOMINAL	FINS OFF	0 DEG
GTF0318	57300	NOMINAL	FINS ON	0 DEG

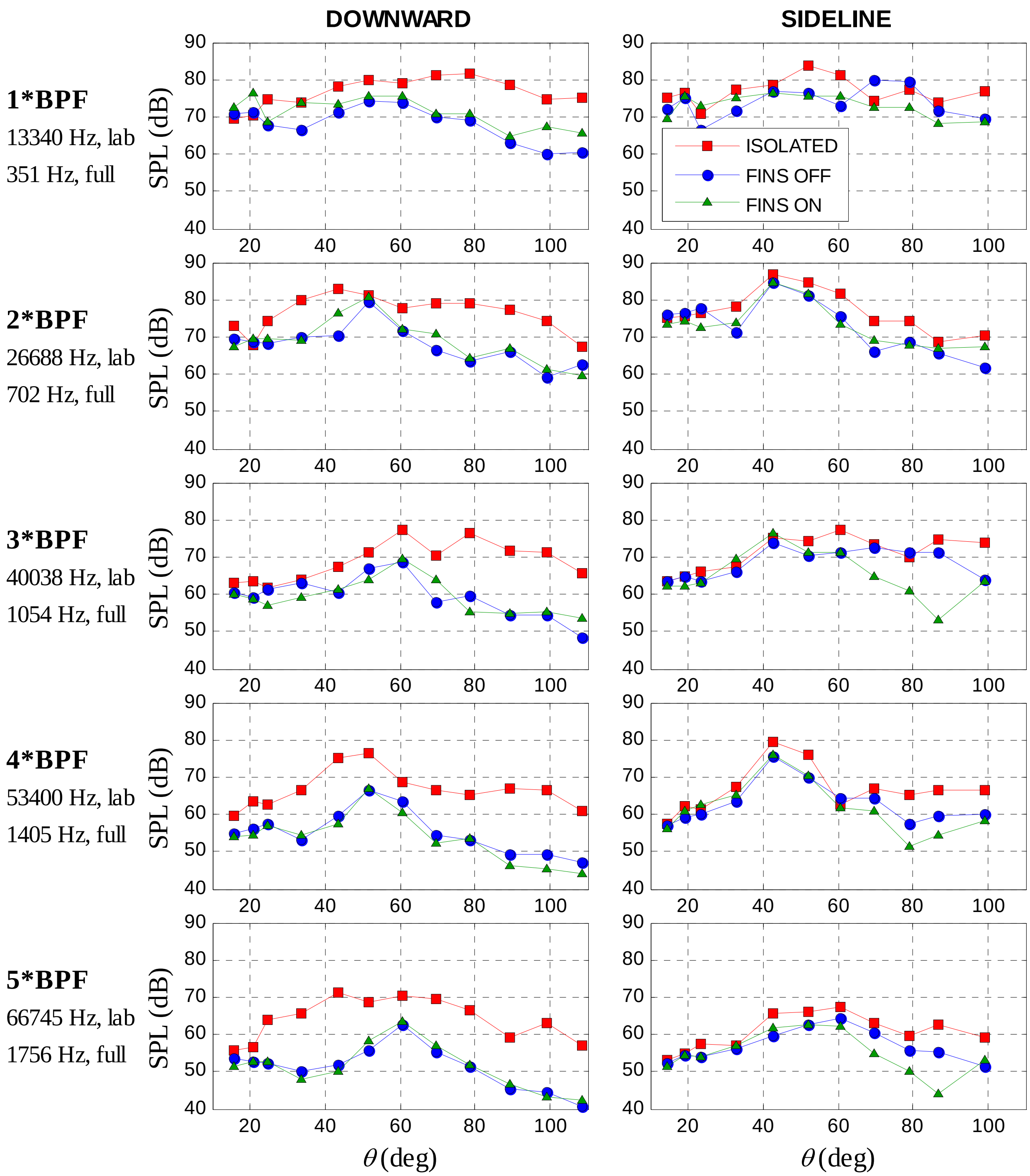

Fig. 14(c) Tone directivity for: isolated ducted fan (red); shielded ducted fan with fins removed (blue); shielded ducted fan with fins installed (green). Engine at nominal axial location. Elevon angle = 0°.

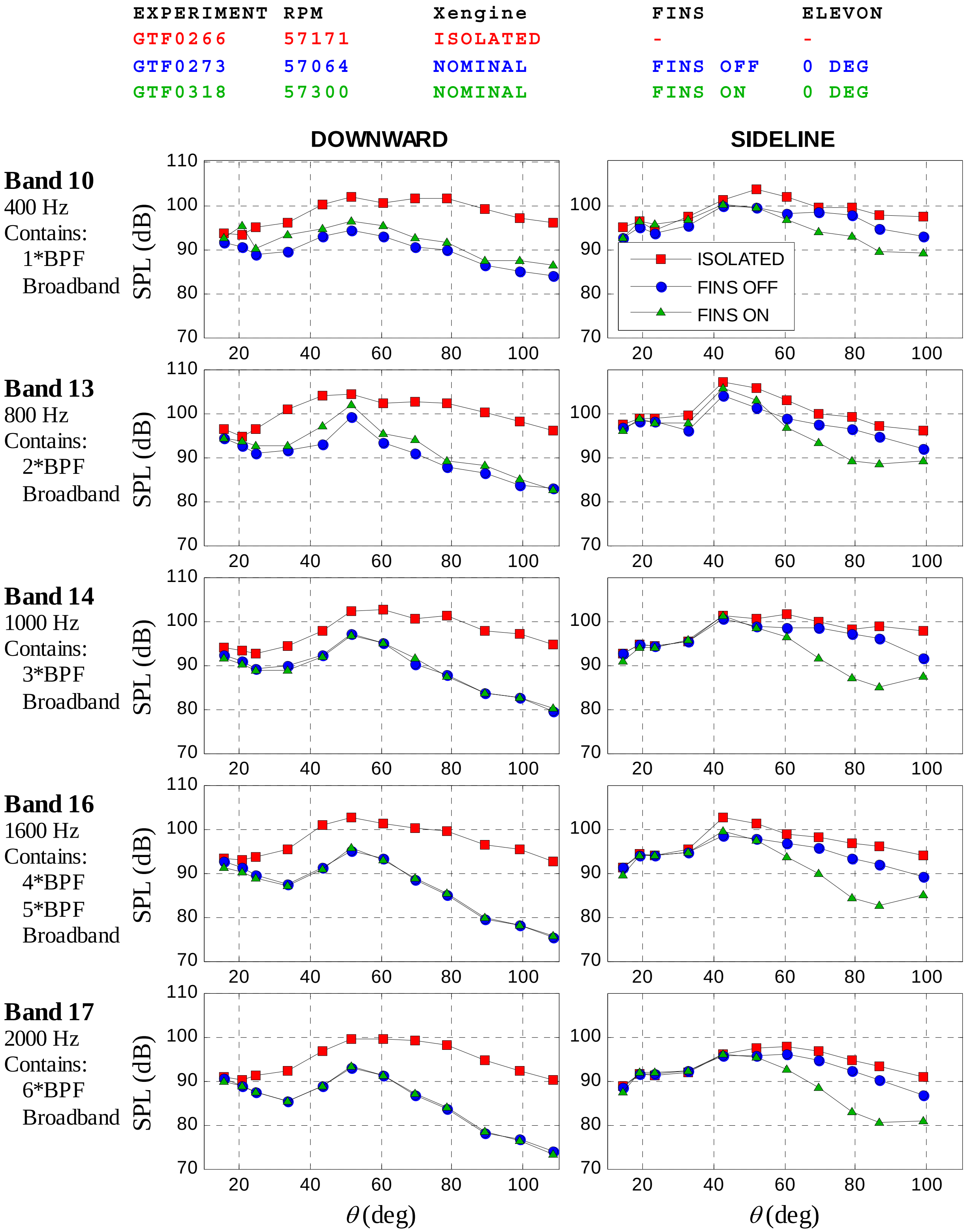

Fig. 14(d) 1/3-octave band directivity for: isolated ducted fan (red); shielded ducted fan with fins removed (blue); shielded ducted fan with fins installed (green). Engine at nominal axial location. Elevon angle = 0°.

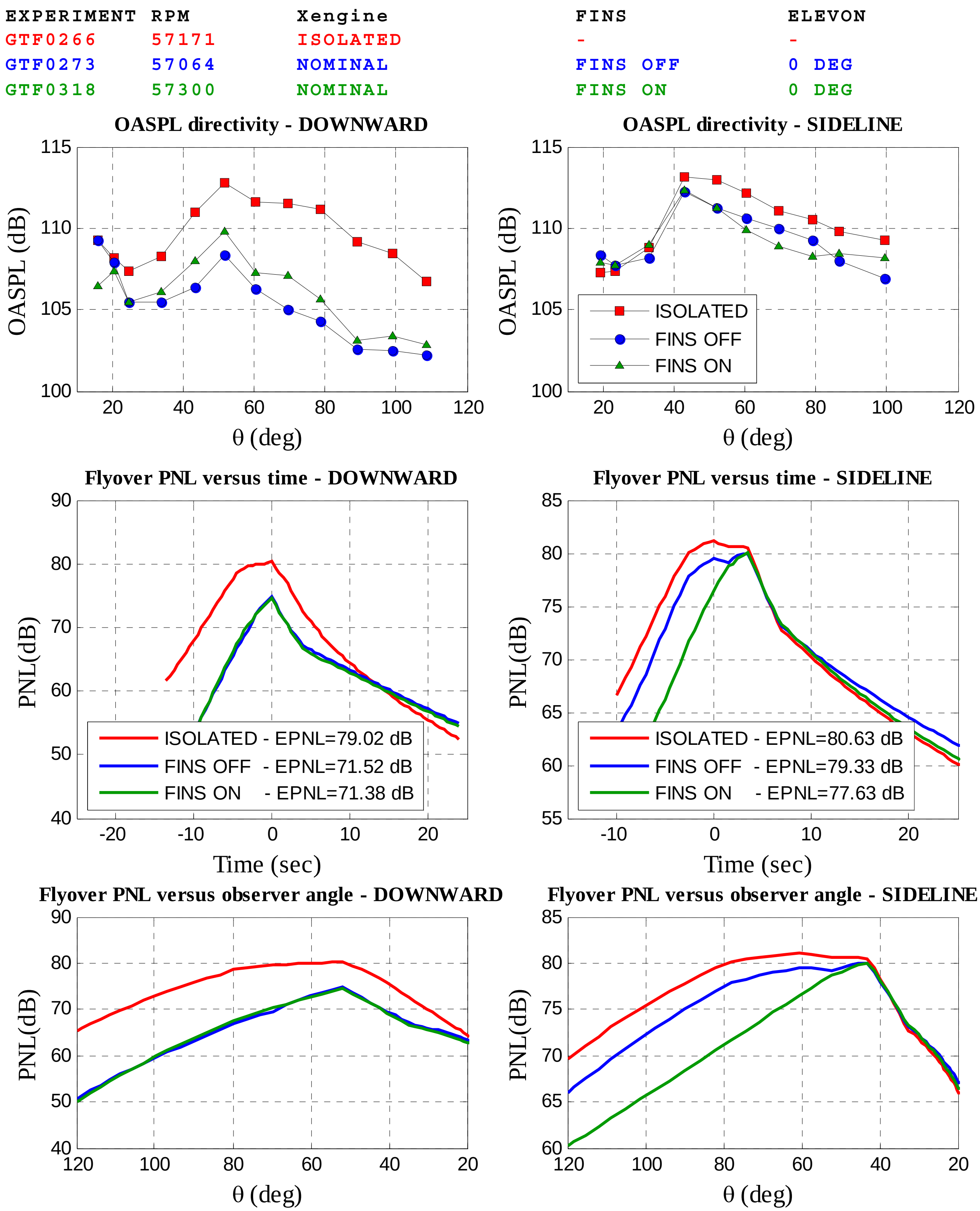

Fig. 14(e) OASPL directivity, PNL time history, PNL versus observer polar angle, and EPNL estimates for: isolated ducted fan (red); shielded ducted fan with fins removed (blue); shielded ducted fan with fins installed (green). Engine at nominal axial location. Elevon angle = 0°.

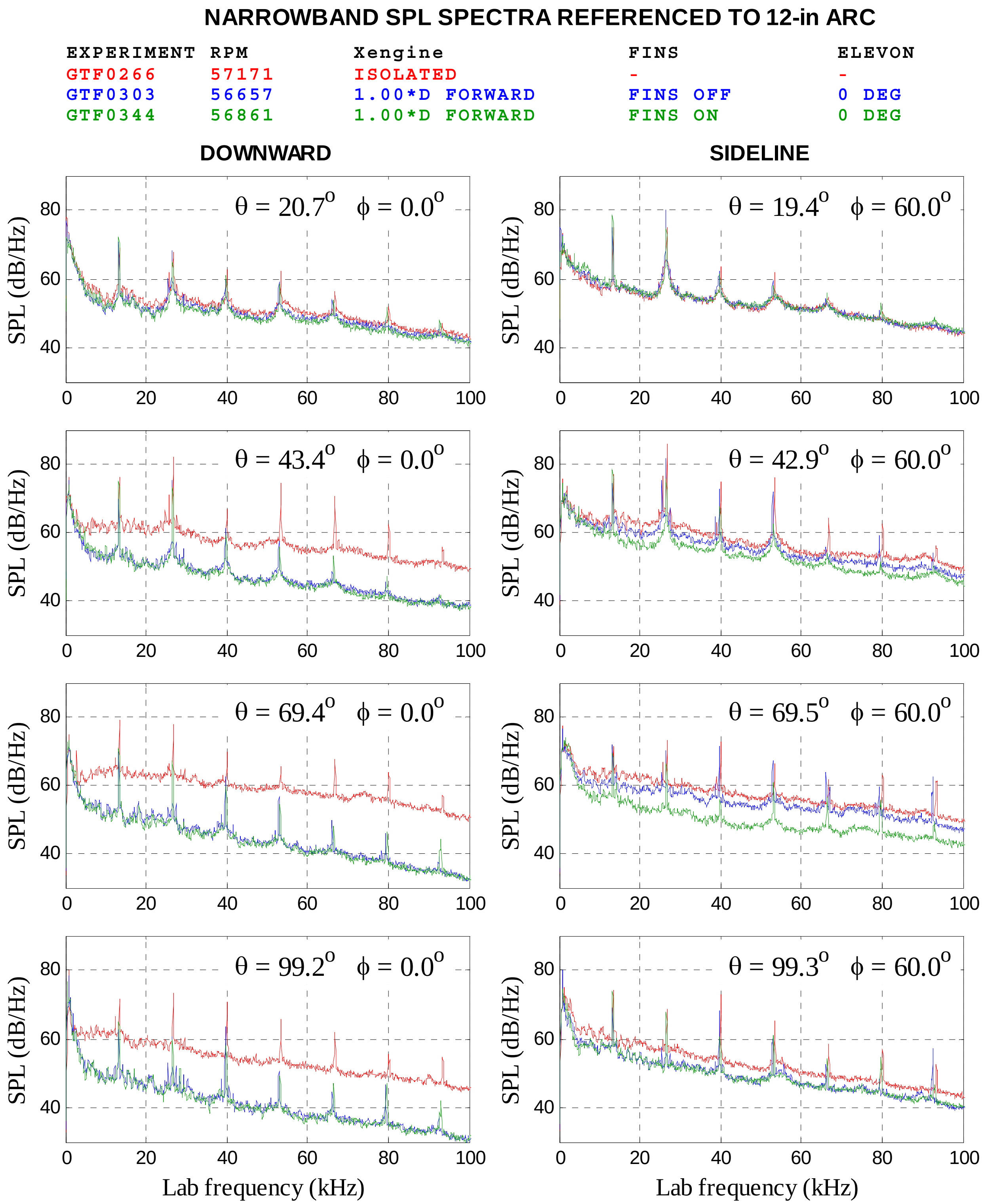

Fig. 15(a) **Narrowband SPL spectra for: isolated ducted fan (red); shielded ducted fan with fins removed (blue); shielded ducted fan with fins installed (green). Engine at 1*D upstream of nominal axial location. Elevon angle = 0°.**

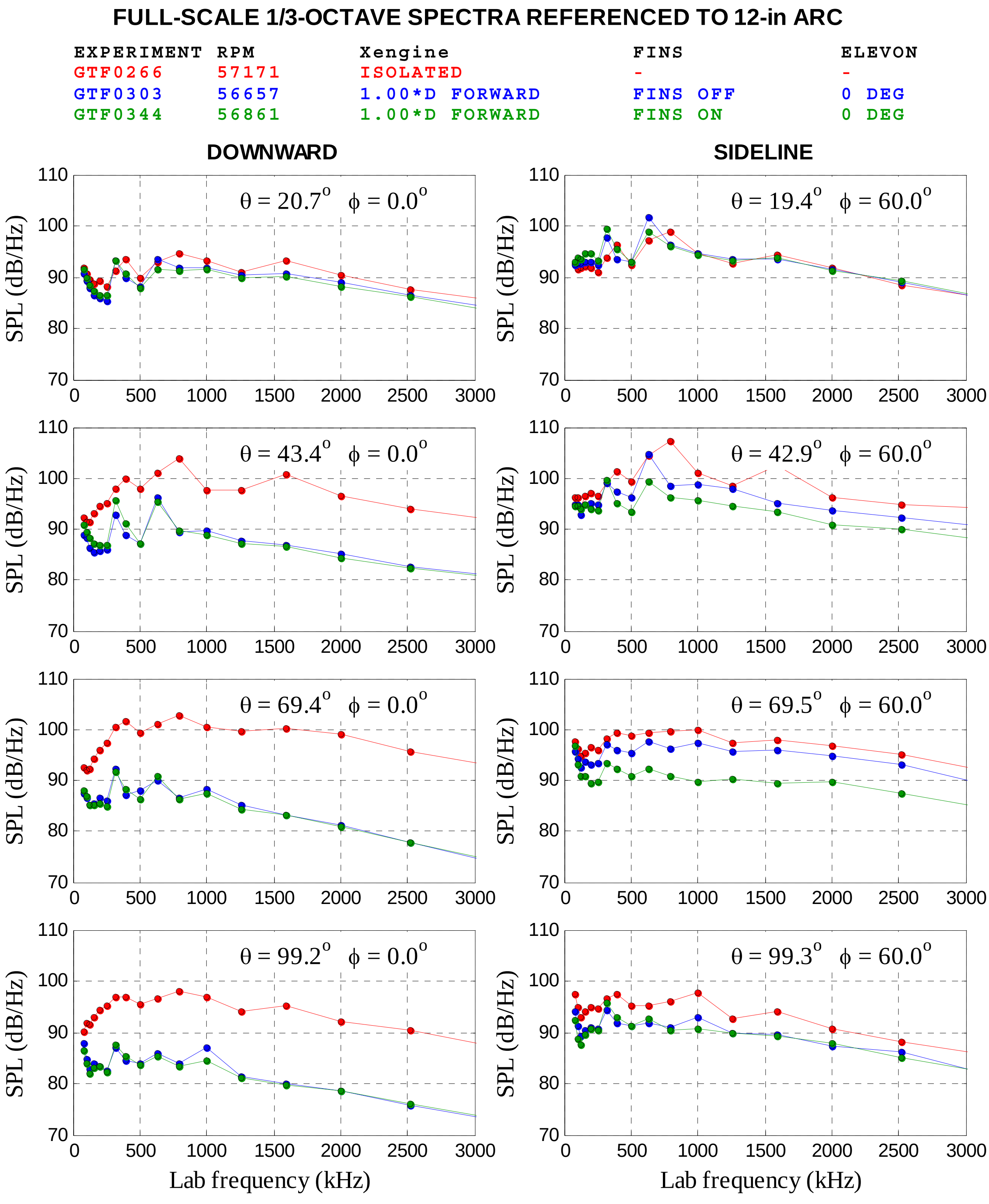

Fig. 15(b) **Full-scale 1/3-octave spectra for: isolated ducted fan (red); shielded ducted fan with fins removed (blue); shielded ducted fan with fins installed (green). Engine at 1*D upstream of nominal axial location. Elevon angle = 0°.**

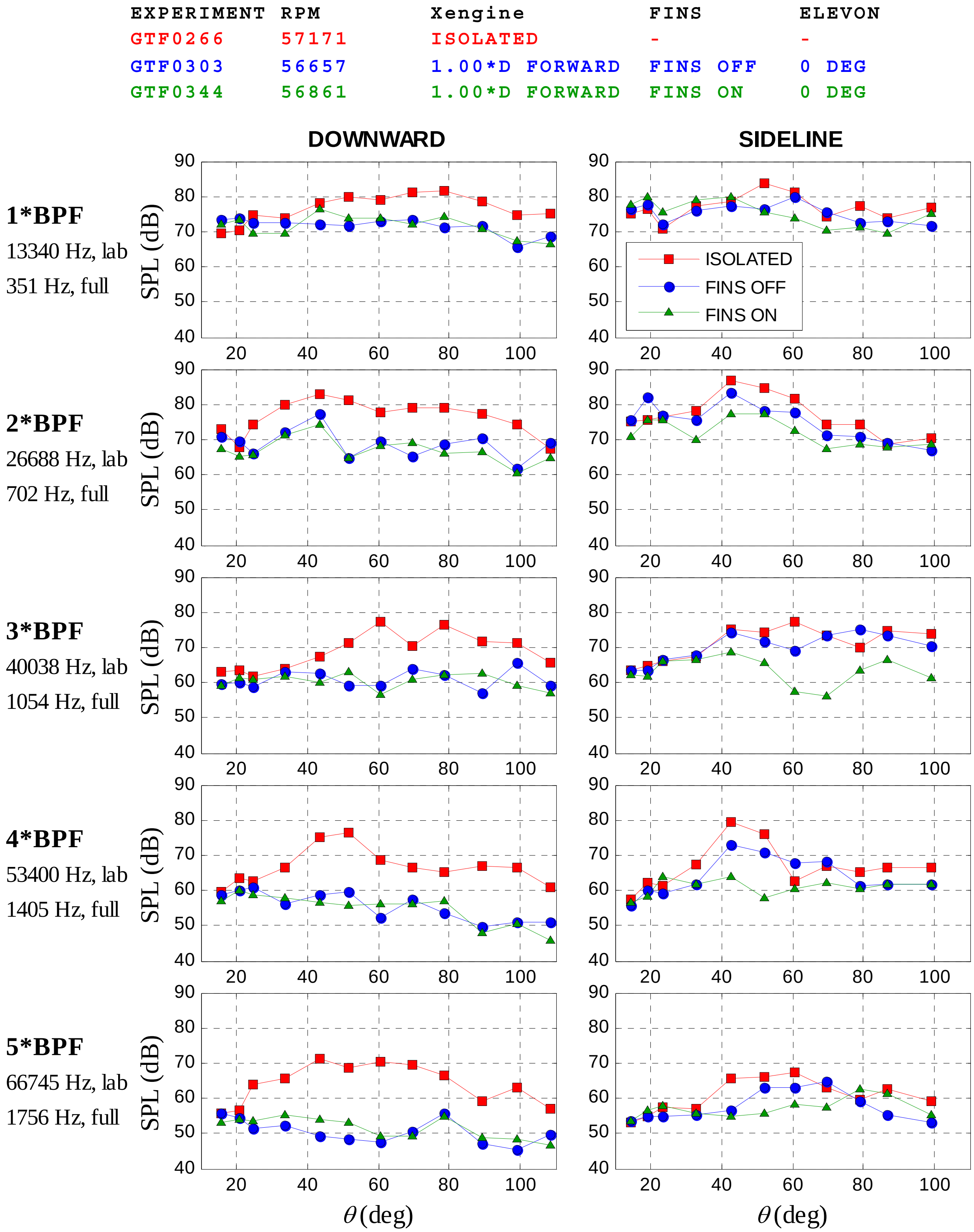

Fig. 15(c) Tone directivity for: isolated ducted fan (red); shielded ducted fan with fins removed (blue); shielded ducted fan with fins installed (green). Engine at 1*D upstream of nominal axial location. Elevon angle = 0°.

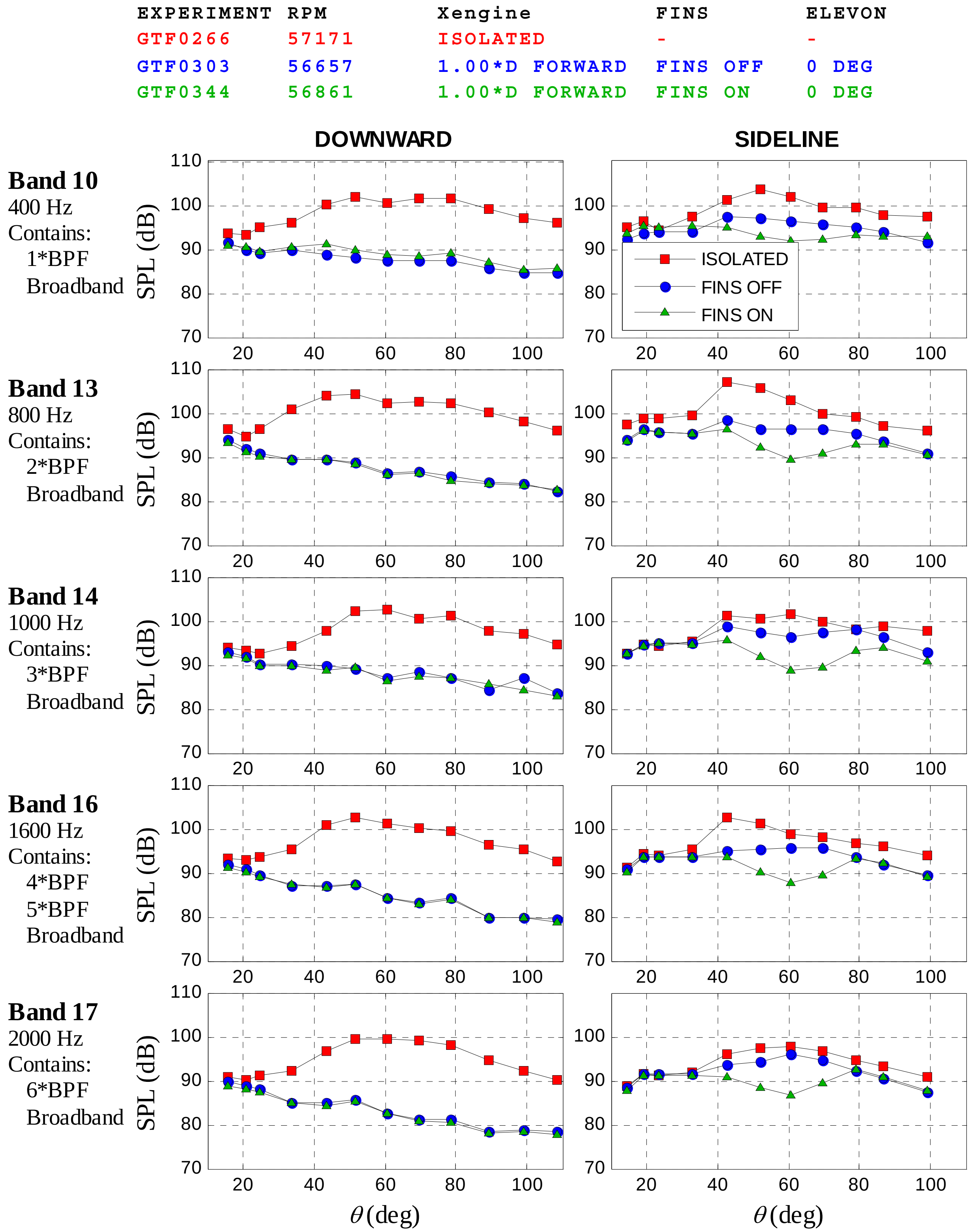

Fig. 15(d) 1/3-octave band directivity for: isolated ducted fan (red); shielded ducted fan with fins removed (blue); shielded ducted fan with fins installed (green). Engine at 1*D upstream of nominal axial location. Elevon angle = 0^o.

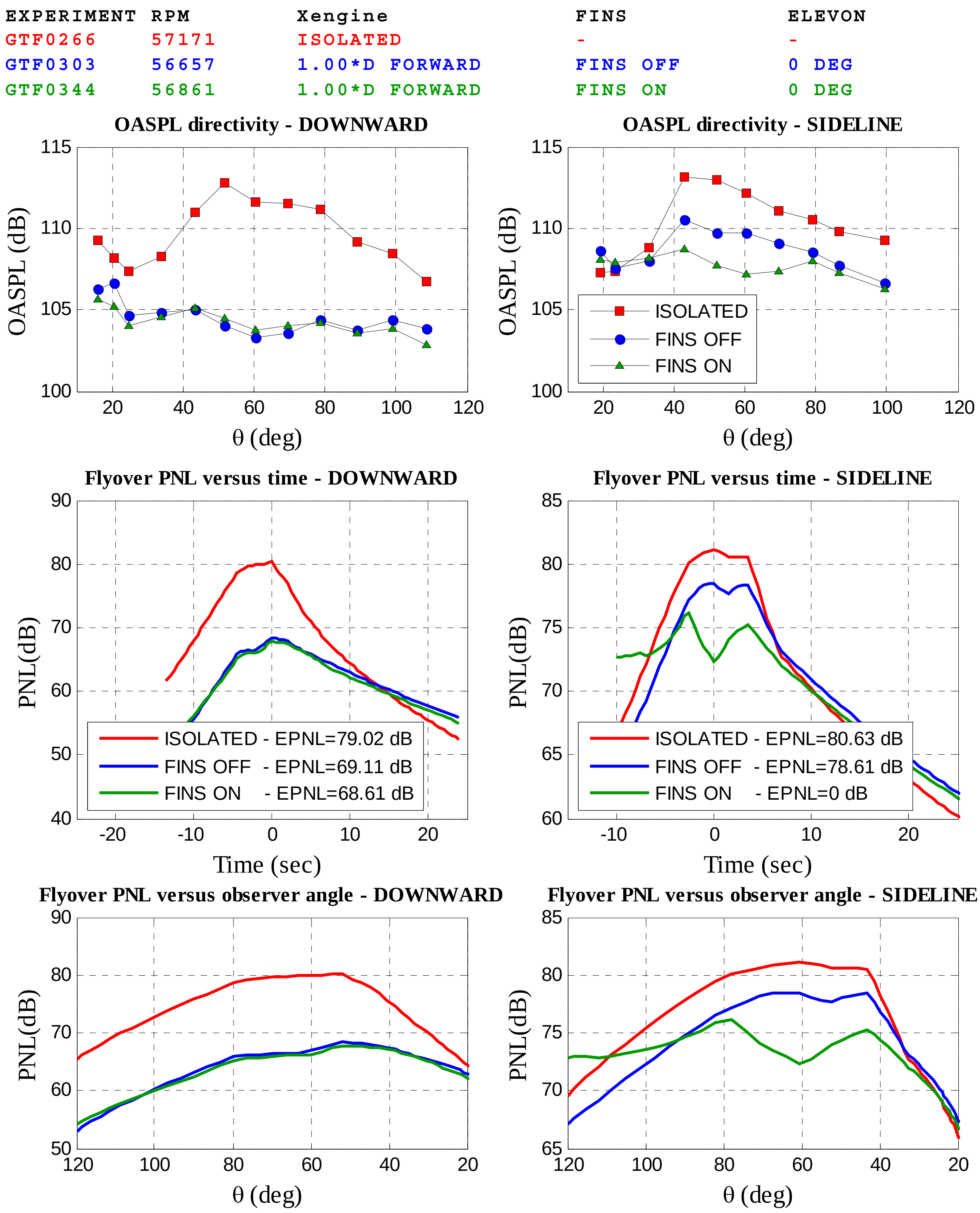

Fig. 15(e) OASPL directivity, PNL time history, PNL versus observer polar angle, and EPNL estimates for: isolated ducted fan (red); shielded ducted fan with fins removed (blue); shielded ducted fan with fins installed (green). Engine at 1*D upstream of nominal axial location. Elevon angle = 0°. EPNL=0 dB indicates that EPNL was not resolved.

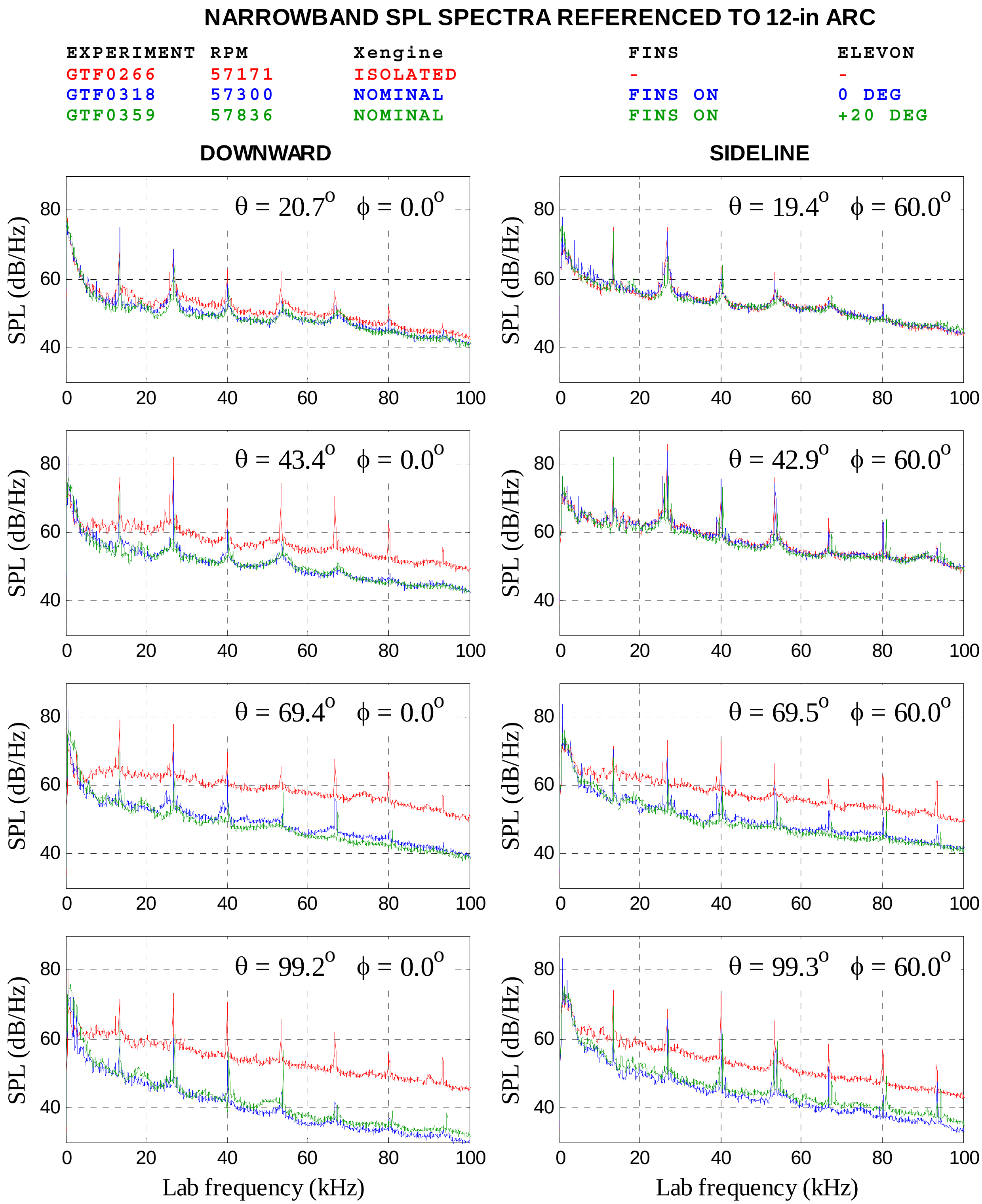

Fig. 16(a) Effect of elevon angle on shielding. Narrowband SPL spectra for: isolated ducted fan (red); shielded ducted fan with elevon at 0° (blue); shielded ducted fan with elevon up at 20° (green). Engine at nominal axial location. Fins are installed.

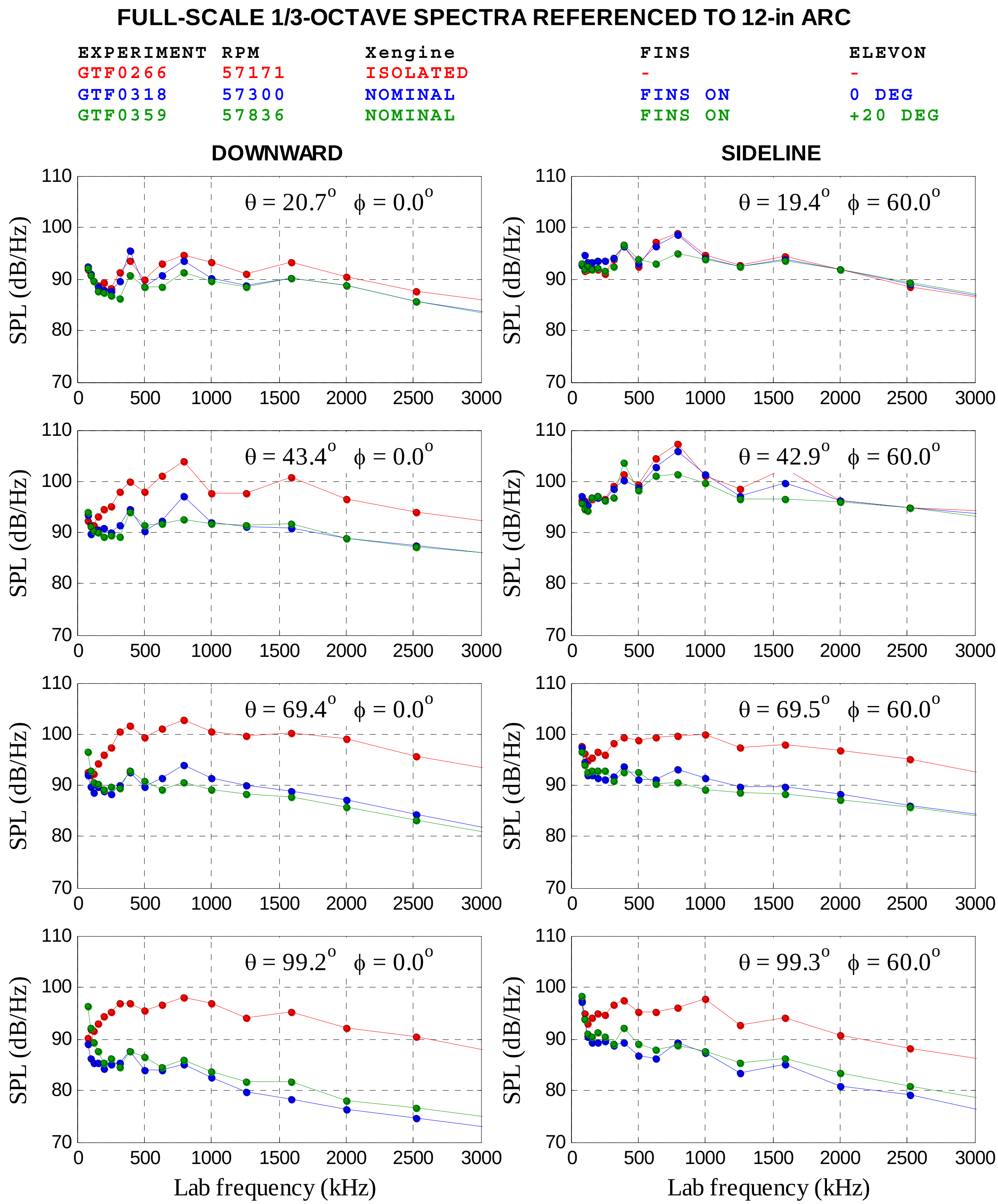

Fig. 16(b) Effect of elevon angle on shielding. Full-scale 1/3-octave spectra for: isolated ducted fan (red); shielded ducted fan with elevon at 0° (blue); shielded ducted fan with elevon up at 20° (green). Engine at nominal axial location. Fins are installed.

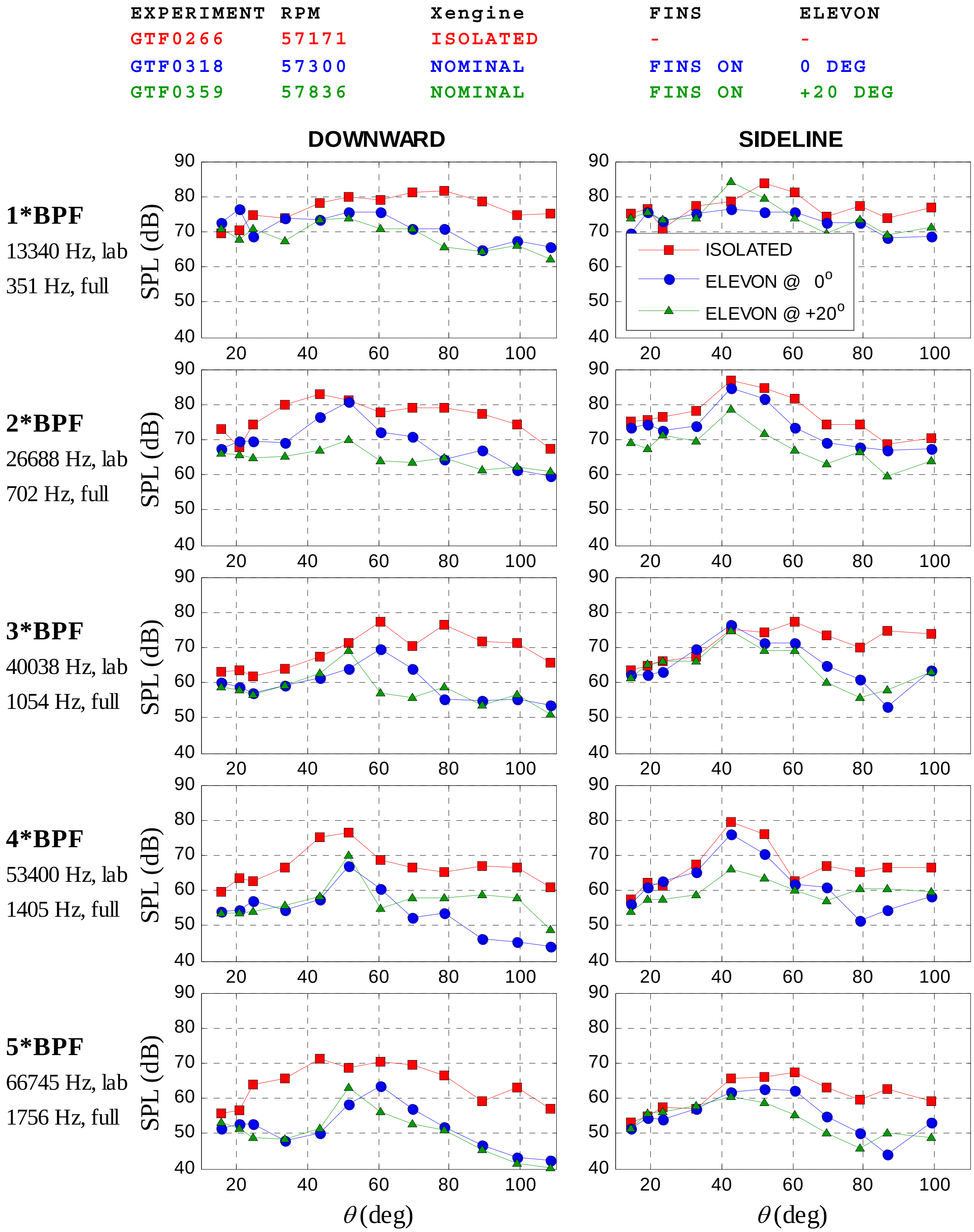

Fig. 16(c) Effect of elevon angle on shielding. Tone directivity for: isolated ducted fan (red); shielded ducted fan with elevon at 0° (blue); shielded ducted fan with elevon up at 20° (green). Engine at nominal axial location. Fins are installed.

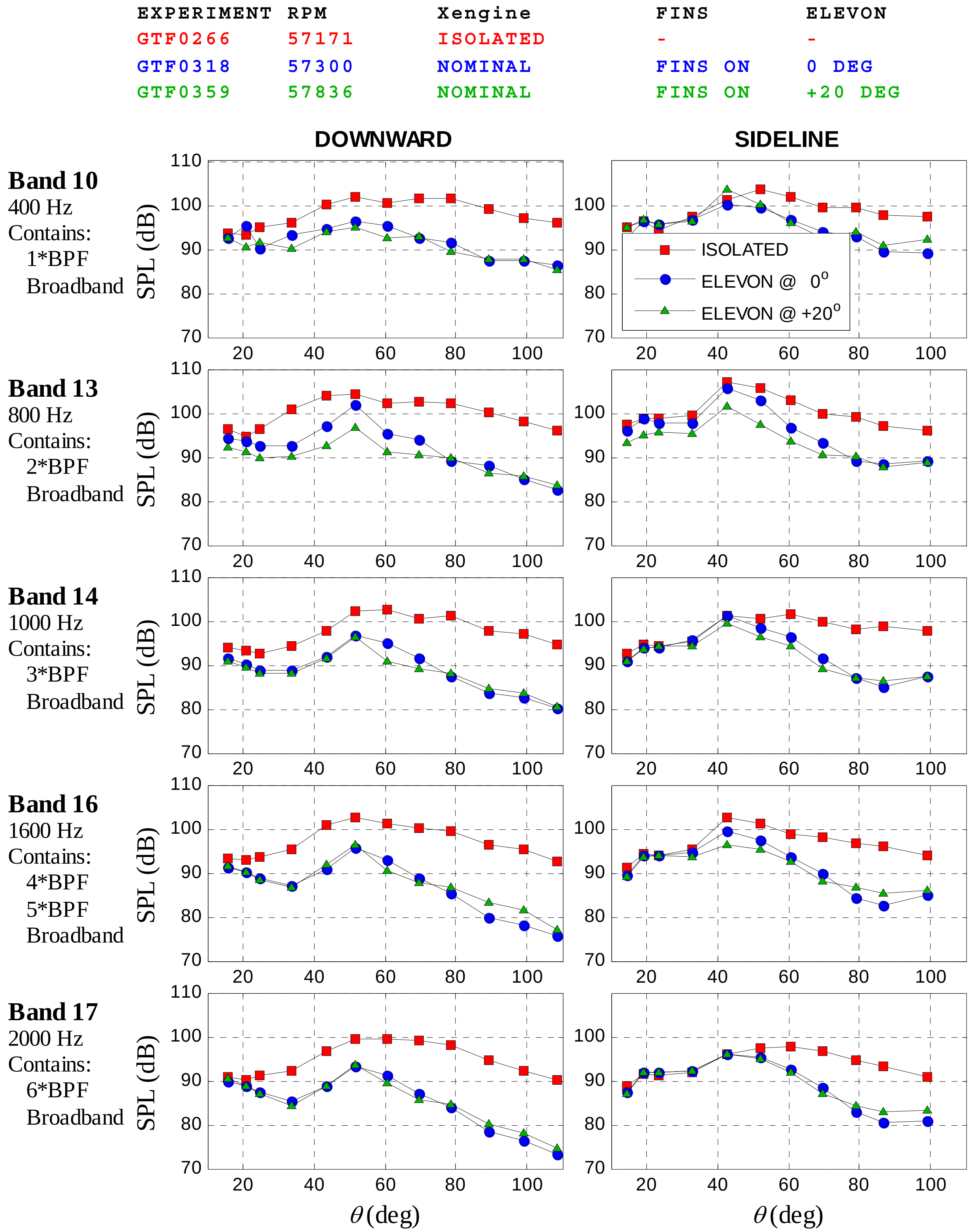

Fig. 16(d) Effect of elevon angle on shielding. 1/3-octave band level directivity for: isolated ducted fan (red); shielded ducted fan with elevon at 0° (blue); shielded ducted fan with elevon up at 20° (green). Engine at nominal axial location. Fins are installed.

EXPERIMENT	RPM	Xengine	FINS	ELEVON
GTF0266	57171	ISOLATED	-	-
GTF0318	57300	NOMINAL	FINS ON	0 DEG
GTF0359	57836	NOMINAL	FINS ON	+20 DEG

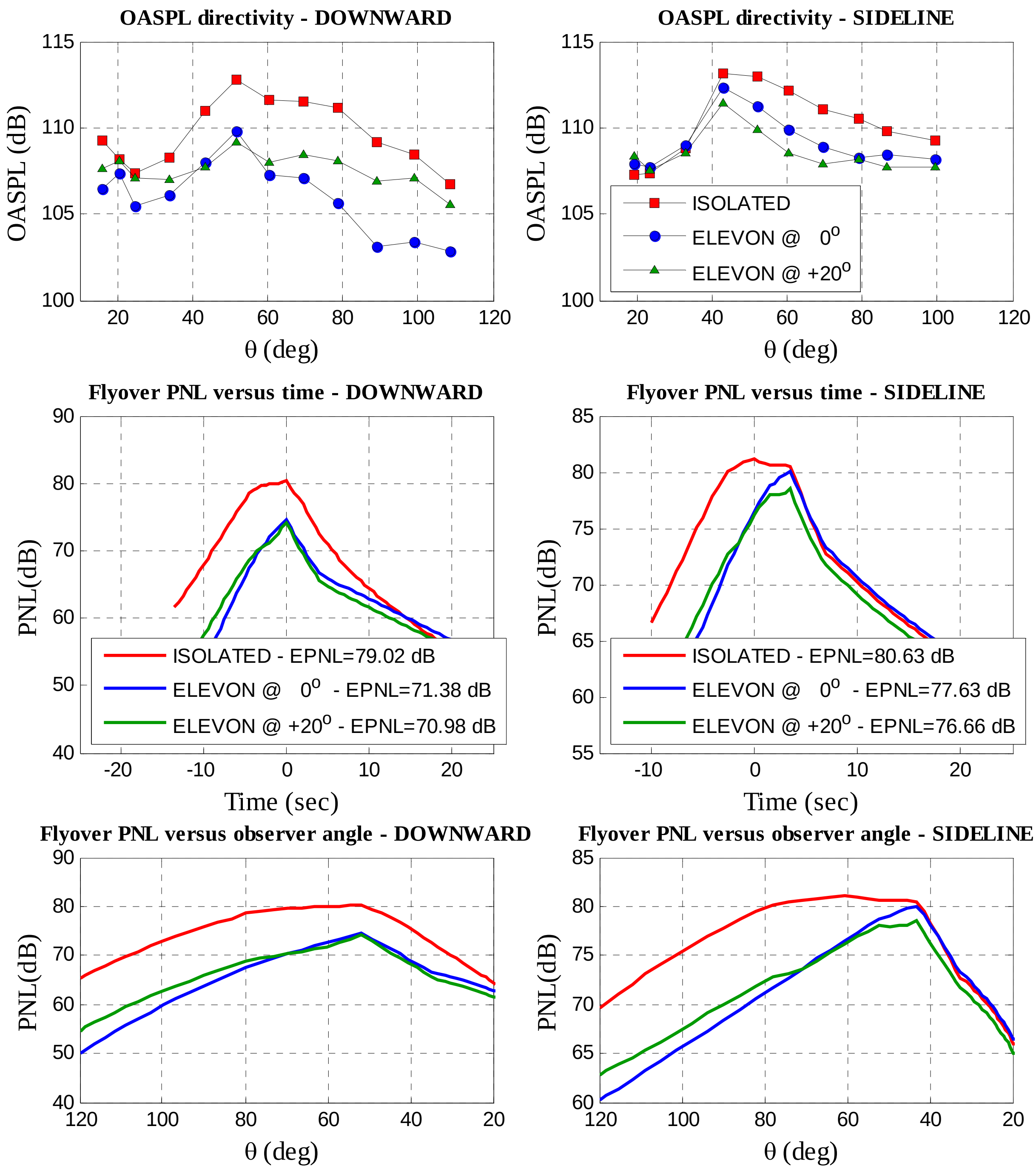

Fig. 16(e) Effect of elevon angle on shielding. OASPL directivity, PNL time history, PNL versus observer polar angle, and EPNL estimates for: isolated ducted fan (red); shielded ducted fan with elevon at 0° (blue); shielded ducted fan with elevon up at 20 deg. (green). Engine at nominal axial location. Fins are installed.

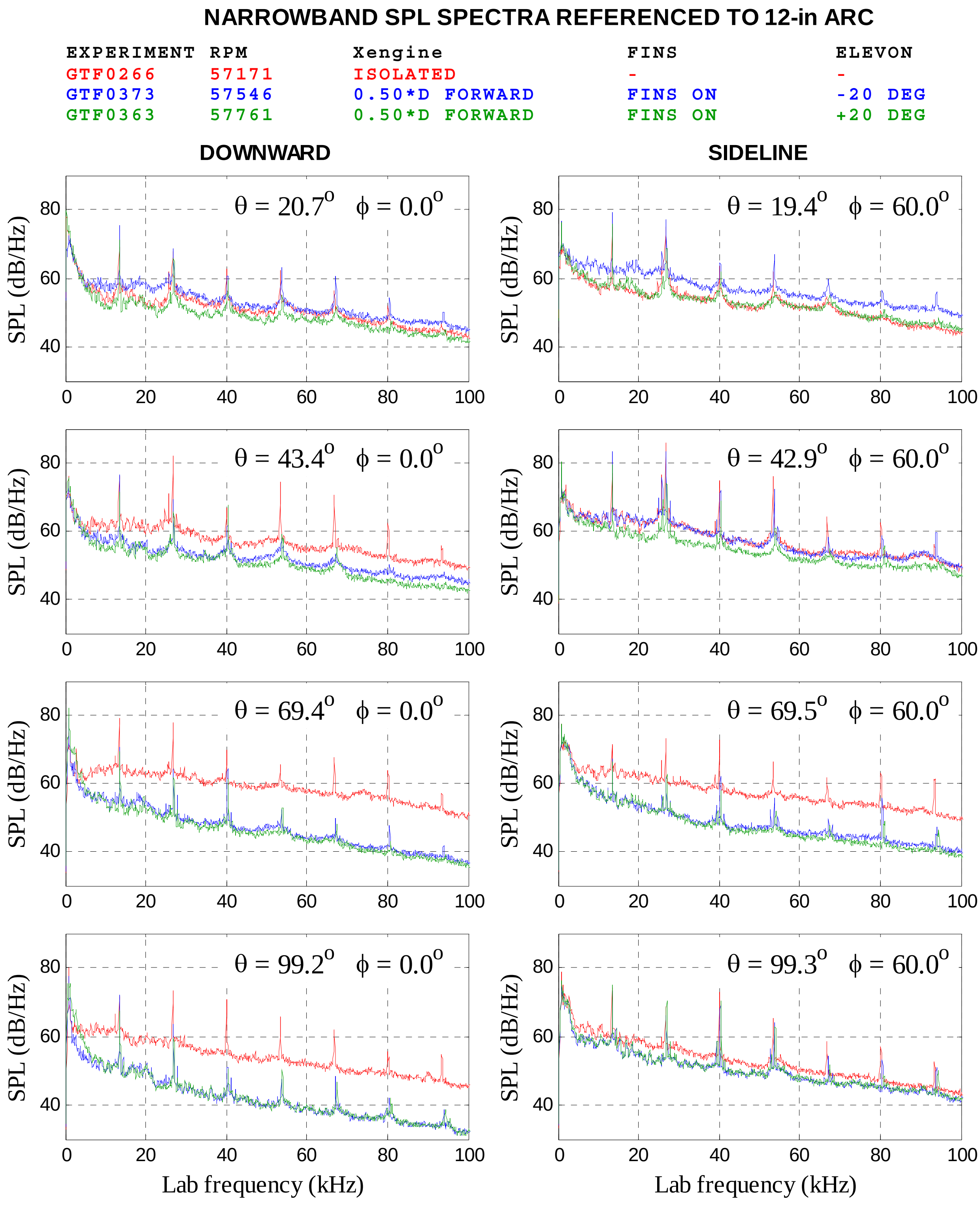

Fig. 17(a) Effect of elevon angle on shielding. Narrowband SPL spectra for: isolated ducted fan (red); shielded ducted fan with elevon down at -20° (blue); shielded ducted fan with elevon up at 20° (green). Engine at 0.5*D upstream of nominal axial location. Fins are installed.

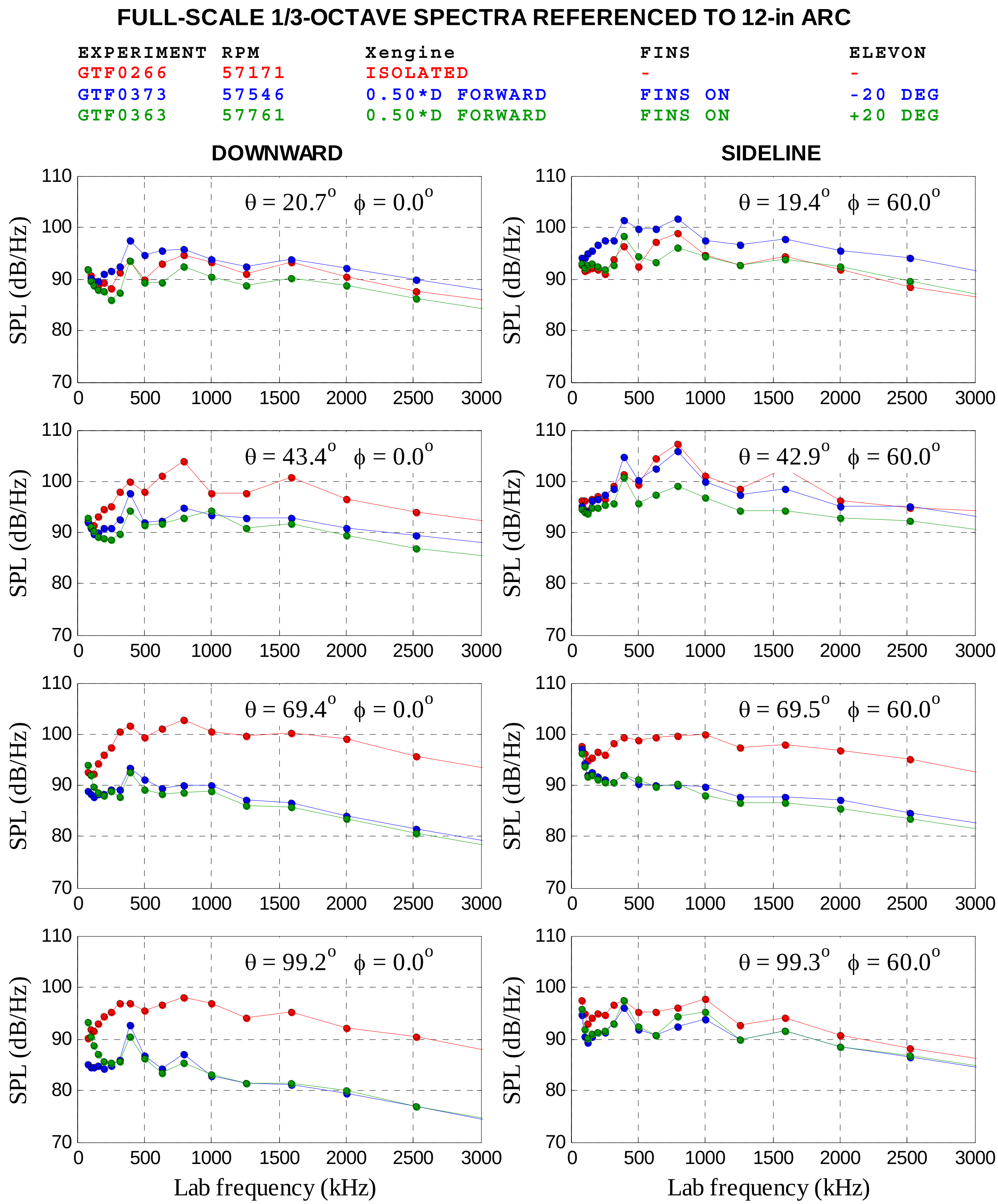

Fig. 17(b) Effect of elevon angle on shielding. Full-scale 1/3-octave spectra for: isolated ducted fan (red); shielded ducted fan with elevon down at -20° (blue); shielded ducted fan with elevon up at 20° (green). Engine at 0.5*D upstream of nominal axial location. Fins are installed.

EXPERIMENT	RPM	Xengine	FINS	ELEVON
GTF0266	57171	ISOLATED	-	-
GTF0373	57546	0.50*D FORWARD	FINS ON	-20 DEG
GTF0363	57761	0.50*D FORWARD	FINS ON	+20 DEG

1*BPF
13340 Hz, lab
351 Hz, full

2*BPF
26688 Hz, lab
702 Hz, full

3*BPF
40038 Hz, lab
1054 Hz, full

4*BPF
53400 Hz, lab
1405 Hz, full

5*BPF
66745 Hz, lab
1756 Hz, full

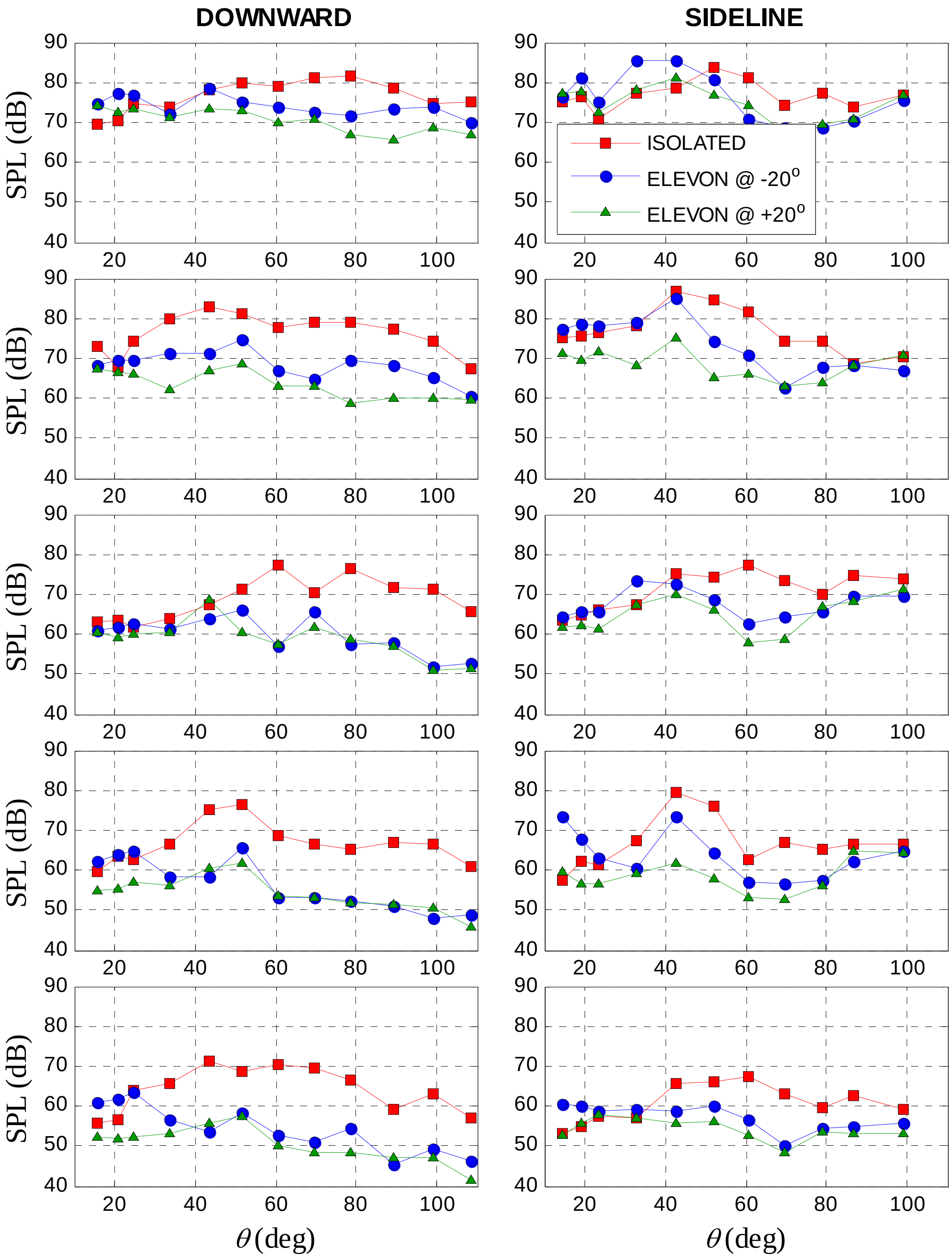

Fig. 17(c) Effect of elevon angle on shielding. Tone directivity for: isolated ducted fan (red); shielded ducted fan with elevon down at -20° (blue); shielded ducted fan with elevon up at 20° (green). Engine at 0.5*D upstream of nominal axial location. Fins are installed.

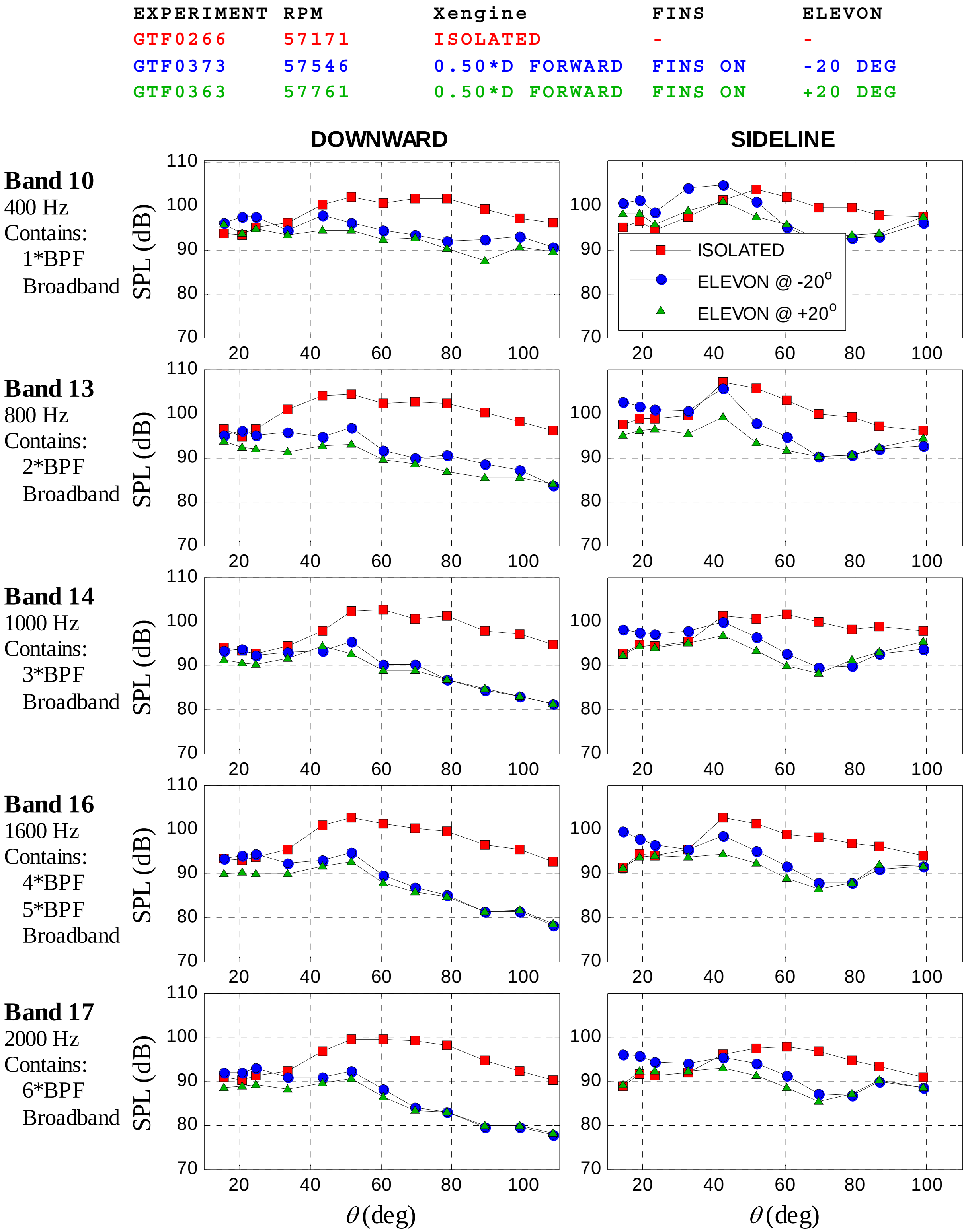

Fig. 17(d) Effect of elevon angle on shielding. 1/3-octave band level directivity for: isolated ducted fan (red); shielded ducted fan with elevon down at -20° (blue); shielded ducted fan with elevon up at 20° (green). Engine at 0.5*D upstream of nominal axial location. Fins are installed.

EXPERIMENT	RPM	Xengine	FINS	ELEVON
GTF0266	57171	ISOLATED	-	-
GTF0373	57546	0.50*D FORWARD	FINS ON	-20 DEG
GTF0363	57761	0.50*D FORWARD	FINS ON	+20 DEG

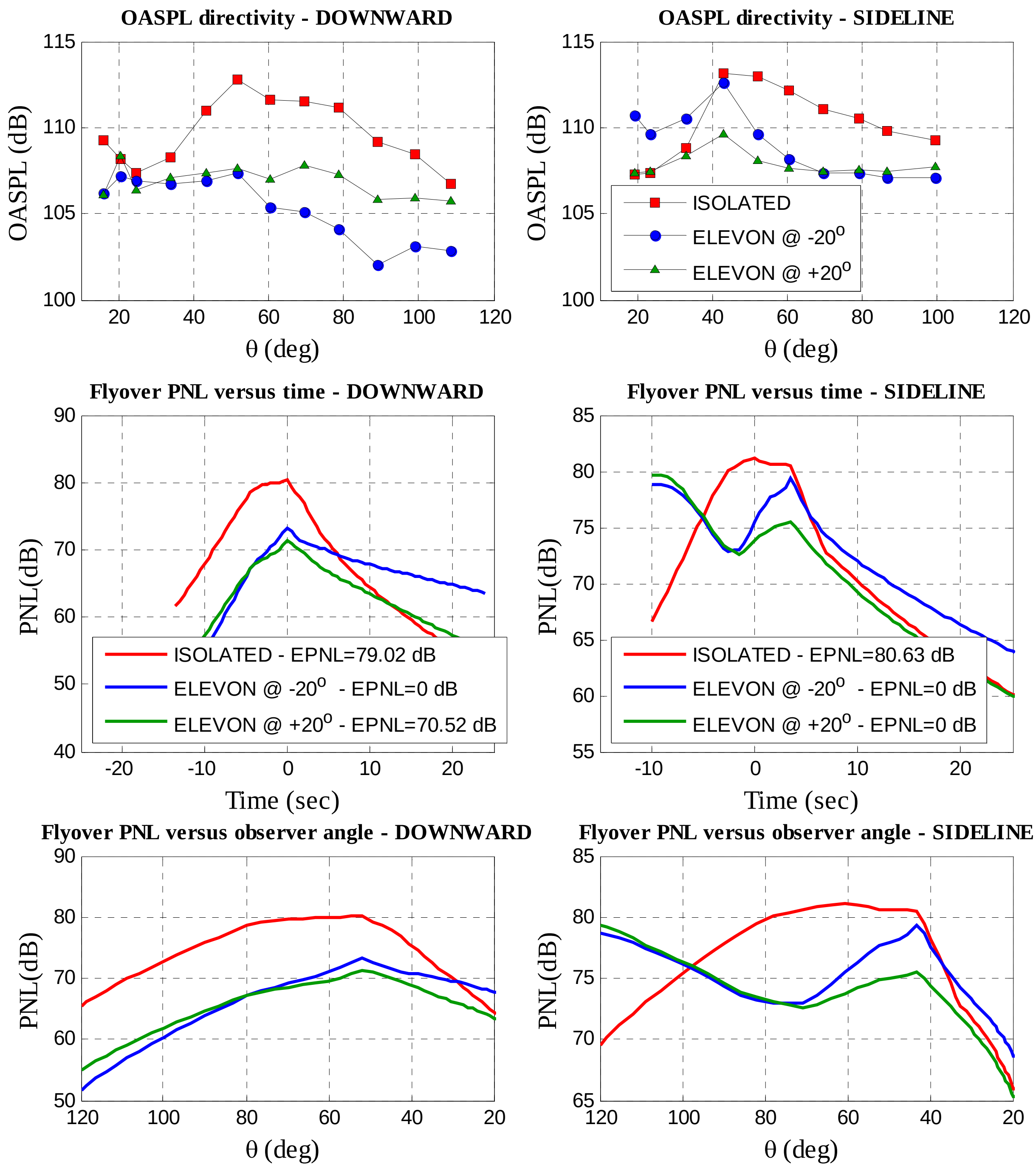

Fig. 17(e) Effect of elevon angle on shielding. OASPL directivity, PNL time history, PNL versus observer polar angle, and EPNL estimates for: isolated ducted fan (red); shielded ducted fan with elevon down at -20^{o} (blue); shielded ducted fan with elevon up at 20^{o} (green). Engine at 0.5*D upstream of nominal axial location. Fins are installed.

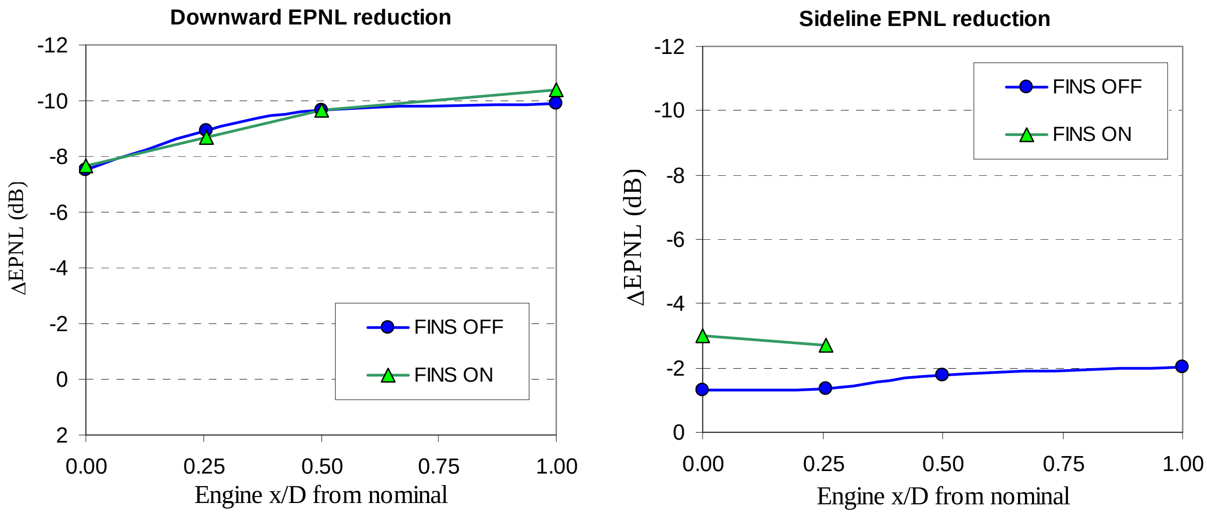

Fig. 18 EPNL reduction versus nacelle axial position for zero elevon angle.

VI. Comparison with Past Larger-Scale Data for Isolated Fan

To assess the relevance of UCI's small-scale tests, it is instructive to compare acoustic trends with available data in the literature for similar ducted fan configurations. Only the isolated fan is considered here because there are no published data of the fan interacting with a BWB-shaped shield. Comparisons are made with the Advanced Ducted Propulsor Fan 1 (ADP1) tests of Woodward[13]; and the Allison Fan tests of Woodward *et al.* [14].

Figure 19 compares the acoustic power level (PWL) of the UCI tests with the ADP1 tests. The principal fan features and operating conditions are annotated in the figures. For the UCI tests, the PWL was calculated by integrating the narrowband spectra over polar angle. Comparing the UCI and ADP1 acoustic power levels (red lines in both plots), we note very similar tonal content with harmonics up to 8*BPF detectable in both tests. Note that 1*BPF was cut off in the ADP1 tests. The broadband levels decline by about 12 dB/decade in both UCI and ADP1 tests.

Figure 20 compares the OASPL directivity of the UCI and ADP1 tests. Note that the NASA convention for sideline emission angle is used (see figure). Very similar trends are noted for the common range of emission angles. In both tests: the OASPL peaks at sideline emission angles near 120^o; at 80^o, the OASPL is ~ 7 dB below peak level; and at 160^o, the OASPL is ~15 dB below peak level.

Lastly, the directivity of the 1/3-octave band containing the 2*BPF tone is compared in Fig. 21 with the Allison tests. With the exception of the Allison "radial upstream" vane configuration (dark circles -- apparently an unusual geometry), the UCI-Allison trends match very well.

These comparisons, albeit limited, indicate that the small-scale tests capture the main acoustic features of the ducted fan.

UCI (2.67 in. dia.)	
M_{tunnel}	0
V_{tip}	690 ft/s
Rotor count	14
Stator Count	24
Hub/tip	0.42

ADP1 (22 in. dia.)	
M_{tunnel}	0.1
V_{tip}	643 ft/s
Rotor count	18
Stator Count	45
Hub/tip	0.43

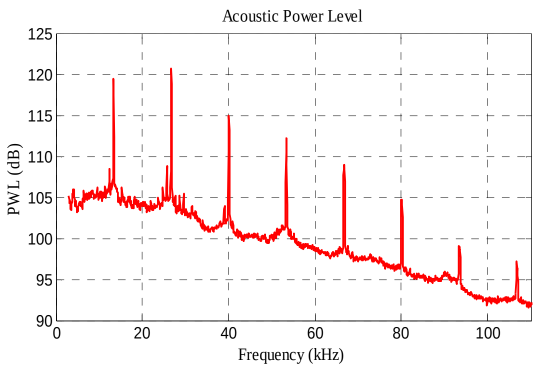

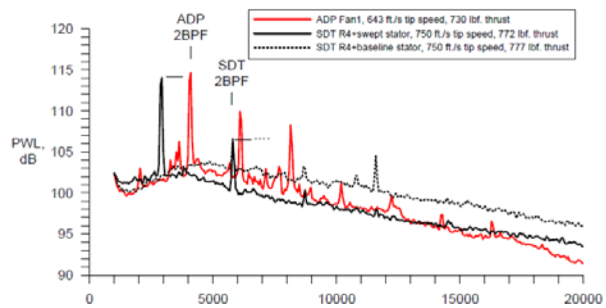

Fig. 19 Comparison of UCI's acoustic power level (PWL) with the ADP1 large-scale tests [13]. Left column presents operating conditions and data for UCI; right column presents operating conditions and data for ADP1. Red curves should be compared.

UCI (2.67 in. dia.)	
M_{tunnel}	0
V_{tip}	690 ft/s
Rotor count	14
Stator Count	24
Hub/tip	0.42

ADP1 (22 in. dia.)	
M_{tunnel}	0.1
V_{tip}	643 ft/s
Rotor count	18
Stator Count	45
Hub/tip	0.43

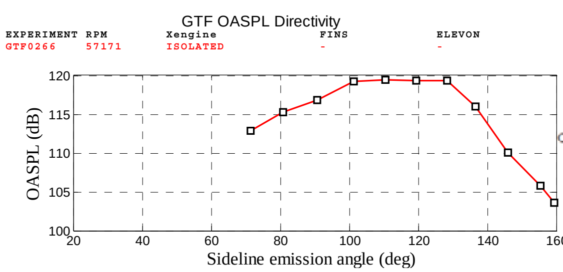

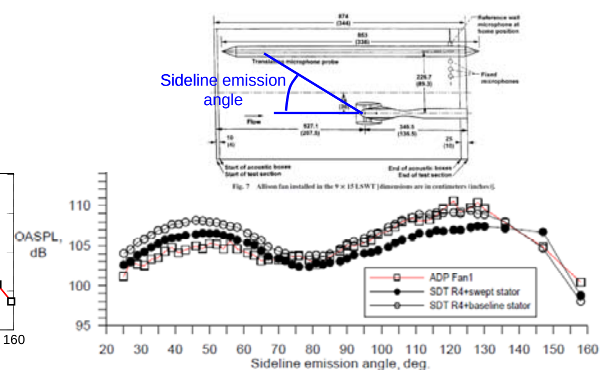

Fig. 20 Comparison of UCI's OASPL directivity with the ADP1 large-scale tests [13]. Sideline emission angle is used as defined in NASA tests (see insert). Left column presents operating conditions and data for UCI; right column presents operating conditions and data for ADP1. Red curves should be compared.

UCI (2.67 in. dia.)	
M_{tunnel}	0
V_{tip}	690 ft/s
Rotor count	14
Stator Count	24
Hub/tip	0.42

Allison (22 in. dia.)	
M_{tunnel}	0.1
V_{tip}	500 ft/s
Rotor count	18
Stator Count	42
Hub/tip	0.30

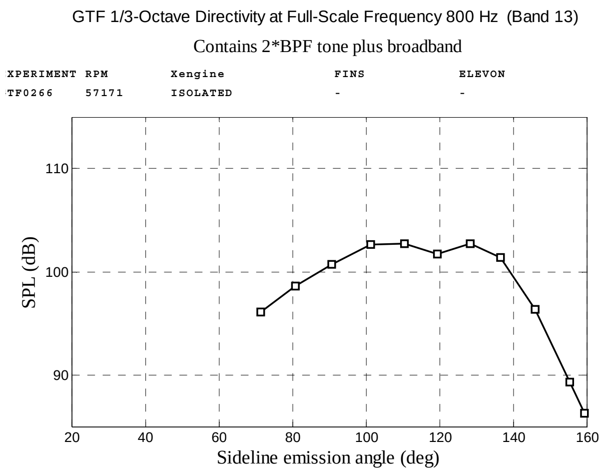

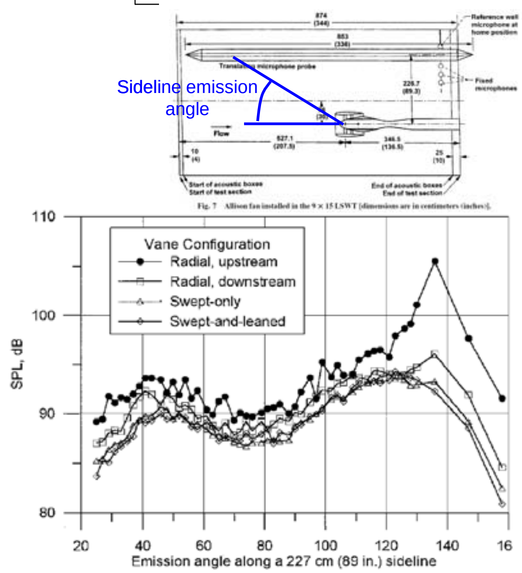

Fig. 12 One-third octave directivities along a 227-cm (89-in.) sideline (50% fan design speed, two BPF tone).

Fig. 21 Comparison of UCI's directivity of band level containing 2*BPF with the Allison large-scale tests [14]. Sideline emission angle is used as defined in NASA tests (see insert). Left column presents operating conditions and data for UCI; right column presents operating conditions and data for Allison.

VII. Concluding Remarks

This project demonstrated the feasibility of simulating the aerodynamics and acoustics of ducted fans using small-scale components (approximately 1/38th scale). Enabling technologies include high-definition stereolithography and high-performance, compact DC brushless motors used in model aircraft. The subscale ducted fan featured a 14-bladed rotor and 24 stators, and operated at fan pressure ratio of 1.15 and rotor tip Mach number of 0.61. Its operation was thus representative of future geared turbofan (GTF) engines with very large bypass ratio. The acoustic results of the isolated ducted fan compare favorably with past large-scale experiments. In addition, the project provided initial data on the shielding of ducted-fan noise using a surface that approximated the shape of the blended wing body airplane (specifically, Boeing's BWB 2025-0009A model). The BWB-shaped shield featured removable fins and a moveable elevon. It translated axially to enable various positions of the nacelle relative to the elevon trailing edge.

The acoustic results with shield installed can be summarized as follows:

- Substantial noise reductions was measured in the downward direction (plane of symmetry of the aircraft). The EPNL reduction ranged from 7.6 dB with the engine at its nominal location to 10.4 dB with the engine moved forward one fan diameter. The fins had minor impact on the downward EPNL.
- Sideline EPNL reduction was marginal with the fins off (approximately 1.5 dB with the engine at nominal position). Installation of the fins improved the sideline EPNL reduction to about 3.0 dB.
- The limited extent of the fins created a finite "shadow zone" in the direction of the sideline observer. The shadow zone can create an unusual time history of PNL which results in a large duration penalty even though the peak PNL level is significantly reduced. There is potential for optimization of the fin design to alleviate this adverse effect and reduce further the sideline EPNL.
- Upward 20^{o} deflection of the elevon improved moderately the shielding, adding 0.4 dB and 1.0 dB to the EPNL reductions in the downward and sideline directions, respectively.

Future enhancements to this approach of simulating fan noise include: fabrication of the rotor from metal (e.g., microfine metal casting aluminum) which can triple its structural strength and allow higher RPMs and thus higher tip Mach numbers; nacelle design with removable stators to increase the flexibility of the test setup; boost in motor power to achieve higher fan pressure ratios; and dual-fan testing to more accurately simulate the shielding and capture interaction effects between two engines. The technologies for these improvements are readily available at costs compatible with a university project. With these enhancements in place, a comprehensive parametric study of fan noise shielding would include the effects of fan specifications (e.g., rotor/stator counts), engine placement, and shield design. Of particular interest is the optimization of the fin geometry to suppress sideline noise. Using stereolithography, more realistic representations of the airframe would be possible. In addition to the far-field acoustic surveys, near-field microphone measurements would contribute to development of models for the fan noise source. Such models are needed in scattering predictions of the installed noise.

Acknowledgment

This project was supported by the Boeing Flight Sciences Technology organization in Huntington Beach, CA (Contract 624440 to University of California, Irvine). The authors acknowledge the technical guidance by Boeing and Pratt & Whitney. We also thank Mr. Tae Kim for his assistance with the design and fabrication of the shield.

References

1. Gerhold, C.H., Clark, L.R., Dunn, M.H., and Tweed, J., "Investigation of Acoustical Shielding by a Wedge-Shaped Airframe," *Journal of Sound and Vibration*, Vol. 294, No. 1–2, June 2006, pp. 49–63.
2. Mayoral, S. and Papamoschou, D., "Effects of Source Redistribution on Jet Noise Shielding," AIAA Paper 2010-0652, Jan. 2010.
3. Thomas, R.H., Burley, C.L., and Olson, E.D., "Hybrid Wing Body Aircraft System Noise Assessment with Propulsion Airframe Aeroacoustic Experiments," AIAA Paper 2010-3913, June 2010.
4. Berton, J. J., "Empennage Noise Shielding Benefits for an Open Rotor Transport," AIAA Paper 2011-2764, June 2011.
5. Truong, A. and Papamoschou, D., "Aeroacoustic Testing of Open Rotors at Very Small Scale," AIAA Paper 2013-0217, Jan. 2013.
6. Liebeck, R.H., "Design of the Blended Wing Body Subsonic Transport," *Journal of Aircraft*, Vol. 41, No. 1, Jan,–Feb. 2004.
7. Topol, A., Ingram, C.L., Larkin, M.J., Roche, C.H., and Thulin, R.D., "Advanced Subsonic Technology (AST) 22-Inch Low Noise Research Fan Rig Preliminary Design of ADP-Type Fan 3," NASA/CR-2004-212718, Feb. 2004.
8. Hughes, C.E., Jeracki, R.J., Woodward, R.P., and Miller, C.J., "Fan Noise Source Diagnostic Test - Rotor Alone Aerodynamic Performance Results," NASA/TM-2005-211681 (AIAA-2002-2426), Apr. 2005.
9. Heidelberg, L.J., "Fan Noise Source Diagnostic Test - Tone Model Structure Results," NASA/TM-2002-211594 (AIAA-2002-2428), May 2002.
10. Morin, B.L., "Broadband Fan Noise Prediction System for Turbofan Engines. Volume 1: Setup_BFaNS User's Manual and Developer's Guide," NASA/CR-2010-216898/VOL1, Nov. 2010.
11. Morin, B.L., "Broadband Fan Noise Prediction System for Turbofan Engines. Volume 3: Validation and Test Cases," NASA/CR-2010-216898/VOL3, Nov. 2010.
12. Hughes, C.E. "Aerodynamic Performance of Scale-Model Turbofan Outlet Guide Vanes Designed for Low Noise, NASA/TM-2001-211352 (AIAA-2002-0374), Dec. 2001.

13. Woodward, R. P., “Comparison of Far-Field Noise for Three Significantly Different Model Turbofans,” AIAA Paper 2008-0049, Jan. 2008.

14. Woodward, R.P., Elliott, D.M., Higher, C.E., and Berton, J.J., “Benefits of Swept-and-Leaned Stators for Fan Noise Reduction”, *Journal of Aircraft*, Vol. 38, No.6, 2001.

15. Sutliff, D.L., Brown, C.A., and Walker, B.E., “Hybrid Wing Body Shielding Studies Using an Ultrasonic Configurable Fan Artificial Noise Source Generating Simple Modes,” NASA/TM-2012-0217685 (AIAA-2012-2076), Nov. 2012.

16. Bonet, J.T., “Boeing ERA N+2 Advanced Vehicle Concepts Results”, Key Speech at 50^{th} AIAA Aerospace Sciences Meeting, January 11, 2012.

17. Bass, H. E., Sutherland, L. C., Zuckerwar, A. J., Blackstock, D. T., and Hester, D. M., “Atmospheric Absorption of Sound: Further Developments,” *Journal of the Acoustical Society of America*, Vol. 97, No. 1, 1995, pp. 680–683.

18. McGowan, R. S., and Larson, R. S., “Relationship Between Static, Flight and Simulated Flight Jet Noise Measurements,” *AIAA Journal*, Vol. 22, No. 4, 1984, pp. 460–464.

19. Noise Standards: Aircraft Type and Airworthiness Certification, Federal Aviation Regulations, Federal Aviation Administration, Jan. 2001, Pt. 36.